Mechanical Characterization of Joints in Segmented Tunnel Liners Due to Thrust Jack Loading and Service Loading

FINAL PROJECT REPORT

By

Ziyan Ouyang, Haotian Zheng
Spencer Quiel, Michael Mooney

Clay Naito
Email: cjn3@lehigh.edu
Lehigh University

Lehigh University

Sponsorship
U.S. Department of Transportation
Lehigh University Cost Share Support

For

University Transportation Center for
Underground Transportation Infrastructure
(UTC-UTI)

December 2023

Disclaimer

The contents of this report reflect the views of the authors, who are responsible for the facts and the accuracy of the information presented herein. This document is disseminated in the interest of information exchange. The report is funded, partially or entirely, by a grant from the U.S. Department of Transportation's University Transportation Centers Program. However, the U.S. Government assumes no liability for the contents or use thereof.

1. Report No.LUY6T2	2. Government Accession No.	3. Recipient's Catalog No.	
4. Title and Subtitle Mechanical Characterization of Joints in Segmented Tunnel Liners Due to Thrust Jack Loading and Service Loading		5. Report Date December 2023	
		6. Performing Organization Code	
7. Author(s) Ziyan Ouyang https://orcid.org/0000-0003-0629-687X, Haotian Zheng https //orcid.org/0000-0001-5481-2205, Clay Naito https://orcid.org/0000-0003-3835-8131, Spencer Quiel https://orcid.org/0000-0002-1316-7059, Michael Mooney https://orcid.org/0000-0001-9063-1209		8. Performing Organization Report No. LU-Year6-Task2	
9. Performing Organization Name and Address University Transportation Center for Underground Transportation Infrastructure (UTC-UTI) Tier 1 University Transportation Center Colorado School of Mines Coolbaugh 308, 1012 14th St., Golden, CO 80401		10. Work Unit No. (TRAIS)	
		11. Contract or Grant No. US DOT Grant # 69A3551747118	
12. Sponsoring Agency Name and Address United States of America Department of Transportation Research and Innovative Technology Administration		13. Type of Report and Period Covered Final Report (Oct. 2021 to Dec. 2023)	
		14. Sponsoring Agency Code UTC-UTI Colorado School of Mines	
15. Supplementary Notes: Report also available at: https://zenodo.org/communities/utc-uti			
16. Abstract. A full-scale experimental and numerical modeling study is conducted to assess the mechanical performance of tunnel lining segments and their behavior under different loading conditions. This study found that the observed crack and strain development matched well with the expected damage formation from the FEA. The addition of supplementary periphery reinforcement in the hybrid segment resulted in earlier crack formation but provided additional strength against radial bursting failure under overload conditions. This study also found that radial thrust jack load eccentricity of 38 mm towards the extrados surface did not have a significant influence on the cracking performance caused by bursting stress. This study highlights the nonlinear behavior of SFRC under thrust demand, which generally appears in the transition zone between lower and upper tensile strain limits. Overall, this study provides insights into the behavior of segmental tunnel lining systems and can inform design and maintenance practices to improve tunnel infrastructure performance and safety. Flexural assessment of radial joint rotational behavior is also conducted. This study finds that the Janssen model, which idealizes joint contact, overestimates the rotational stiffness of closed joints at low axial loads and provides overly conservative estimations of rotational stiffness and flexural capacity at large rotation levels. It is suggested that for a better approximation through computational joint models, factors such as skewness, bolts, gasket, effects of confined concrete, and the relationship between joint contact and axial force levels should be considered. This study also concludes that bolting can provide significant rotational stiffness at large joint rotation levels, and it is suggested to reserve bolts at joint locations that might experience large rotation due to earth pressure and other types of loading. This study also finds that the flexural capacity of skewed radial joints is approximately 70% higher than predicted in Janssen's model when subjected to certain axial loads. Finally, the study finds that damage to the joint at large rotations is limited to hairline cracking of the contact surface, with no visible damage on the intrados under these elevated demands, thus limiting the potential for in-situ inspection. The study also finds that the use of SFRC does not prevent the formation of fire-induced spall of the intrados surface of the tunnel line. Additional work is needed to prevent this mode of failure.			
17. Key Words Precast Concrete, Joint Flexure, Thrust Load, Fire, Tunnel, Design		18. Distribution Statement No restrictions.	
19. Security Classification (of this report) Unclassified	20. Security Classification (of this page) Unclassified	21. No of Pages 67	22. Price NA

Table of Contents

List of Figures

List of Tables

Executive Summary

Tunnels provide a critical link within modern transportation networks. In modern tunnel construction, precast segmental tunnel linings installed by TBMs are a common practice. However, the thrust jack load generated during TBM advancement can cause tension and damage to segments that are not properly designed. Additionally, the presence of joints in segmental tunnel linings can contribute to deformation problems. Furthermore, precast drop ceilings in tunnels, which are crucial for ventilation, are more susceptible to damage during intense fire events due to their thinner construction compared to tunnel linings.

Precast segmental tunnel linings are typically installed via a TBM, which advances by thrusting against the previously installed segmental ring. The forces applied through the thrust jack pads can induce significant tensile stresses and strains in the segment via bursting and spalling, and improperly designed segments can suffer from cracking as a result. An experimental study has been conducted to evaluate the progression of damage from initial cracking to ultimate capacity for full-scale PCTL segments under thrust jack loading. The baseline segment design is composed of steel fiber reinforced concrete (SFRC), and the impact of supplemental conventional steel bar reinforcement and load application eccentricity were also investigated.

The tunnel lining segments have sufficient flexural resistance due their substantial thickness; however, the existence of joints in segmental tunnel linings contributes to various deformation problems, as they are considered the weakest components of segmental tunnel linings, where their performance heavily relies on the axial force induced by earth pressure. The joint rotational behavior affects the overall stiffness and performance of tunnel lining ring significantly, so it is generally examined through experiments and numerical models to provide guidance for design. Theoretical models with various assumptions on material behavior have been proposed by researchers to predict the joint rotational behavior. An experimental study was conducted to examine the rotational behaviors of full-scale radial joints with 8° skewness at various axial load levels, and to compare with widely used Janssen's model (*1*). The effects of bolting have also been investigated to determine the viability of bolt removal after tunnel construction completes.

Overall, this report aims to improve the design and construction of tunnel structures and enhance their safety in construction and service, by providing a better understanding of the performance of segmental tunnel linings under various conditions.

Findings

The main contributions of this study are: (1) assessment of PCTL segments under thrust jack load through experimentation and numerical modeling, (2) experimental estimation of the flexural performance of radial joints in segmental tunnel lining systems, and (3) fire induced spall of tunnel linings.

The detailed contributions this report provides are the following:

- The study of PCTL segments under thrust jack load contributes to the understanding of the performance of segmental tunnel lining systems under thrust jack loading. This study conducted full-scale experimentation and numerical modeling to assess the mechanical performance of tunnel lining segments and their behavior under different loading conditions. This study found that the observed crack and strain development matched well with the expected damage formation from the FEA. The addition of supplementary periphery reinforcement in the hybrid segment resulted in earlier crack formation but provided additional strength against radial bursting failure under overload conditions. This study also found that radial thrust jack load eccentricity of 38 mm towards the extrados surface did not have a significant influence on the cracking performance caused by bursting stress. This study highlights the nonlinear behavior of SFRC under thrust demand, which generally appears in the transition zone between lower and upper tensile strain limits. Overall, this study provides insights into the behavior of segmental tunnel lining systems and can inform design and maintenance practices to improve tunnel infrastructure performance and safety.
- The experimental assessment of radial joint rotational behavior provides experimental data on the rotational behavior of skewed radial joint assemblies, as well as the effects of bolting and potential joint damage due to excessive rotation. This study finds that the Janssen model, which idealizes joint contact, overestimates the rotational stiffness of closed joints at low axial loads and provides overly conservative estimations of rotational stiffness and flexural capacity at large rotation levels. It is suggested that for a better approximation through computational joint models, factors such as skewness, bolts, gasket, effects of confined concrete, and the relationship between joint contact and axial force levels should be considered. This study also concludes that bolting can provide significant rotational stiffness at large joint rotation levels, and it is suggested to reserve bolts at joint locations that might experience large rotation due to earth pressure and other types of loading. This study also finds that the flexural capacity of skewed radial joints is approximately 70% higher than predicted in Janssen's model when subjected to certain axial loads. Finally, the study finds that damage to the joint at large rotations is limited to hairline cracking of the contact surface, with no visible damage on the intrados under these elevated demands, thus limiting the potential for in-situ inspection.
- The use of SFRC does not prevent the formation of fire-induced spall of the intrados surface of the tunnel line. Additional work is needed to prevent this mode of failure.

1. Project Scope

Precast segmental tunnel liners (installed via tunnel boring machines or TBMs) have become increasingly used in modern tunnel construction. The performance of the joints (both radial and longitudinal) due to in-plane and out-of-plane loading will influence the response of the liner to fire and blast loading. The Lehigh team is working with Prof. Michael Mooney and the UTC-UTI researchers at CSM in support of an FHWA-funded test program which will have the following objectives: (1) characterize the moment-rotation response and failure modes of the radial joints between segments when subjected to a combination of out-of-plane loading and restraining arching action (i.e. in-plane ring stresses); and (2) evaluate the capacity of the longitudinal joints for thrust jack loading. These tests will be conducted by Prof. Mooney and Lehigh research engineers at Lehigh's Fritz Laboratory with assistance from Profs. Naito and Quiel as well as their graduate student team.

Lehigh's Task 2 for Year 6 of the UTC-UTI will continue the examination of these systems, both at ambient conditions and high temperature. Validation and parametric study of computational models is performed at ambient conditions, with the goal of providing guidance to designers regarding the realistic behavior of these systems in deployment. Additional testing on the spall performance of segments are examined. Steel connections were originally to be examined but based on current practice radial bolts are commonly removed prior to service and do not play a critical role.

This work will establish fundamental understanding of the mechanical response of these joints, which will benefit the tunnel construction community in the design and implementation of these systems. Funding for this task will support the Lehigh research team's development of validated parametric models and interaction with the FHWA-funded experimental program.

2. Full-Scale Testing of Precast Tunnel Lining Segments Under Thrust Jack Loading: Design Limits and Ultimate Response

2.1. Introduction and Background

Segmental PCTL and TBMs have been increasingly adopted for modern tunnel construction to enable rapid construction in various geological conditions. For tunnels constructed using a standard TBM approach, circumferential PCTL rings provide both structural integrity to the bored tunnel cavity and a support against which the TBM can thrust forward. TBM thrust jacks push against the leading edge of previously installed PCTL segments at discrete pad locations during the boring process. Once adequate forward progress is achieved, a new ring of segments is installed via a conveyance and lift system. The segments are precast with a curved rectangular or parallelogram shape, and a trapezoidal key segment used to lock each ring into place. Five or six segments are typically used to form the ring of a transit tunnel with 6-7 m diameter, and 12-14 segments are used to comprise larger roadway or multi-use tunnels at diameters near 12 m.

Forward movement of the TBM can apply very high bearing forces (i.e. thrust jack load) to the exposed circumferential joints of the precast segments (*2*). In many cases, thrust jack load during the tunnel's construction is the most significant load case for the design of these segments (Bakhshi and Nasri 2014) and can range from 1-6 MN per thrust jack pad depending on the tunnel diameter, thrust jack pad layout, and underground conditions. In design, stresses induced by thrust jack loads can be approximated using existing analytical expressions that were developed for estimating anchorage zone stresses in post-tensioned prestressed beams (*4*, *5*). Studies have examined the accuracy of these approaches for estimating the thrust-induced stresses in a tunnel liner (*3*, *6*, *7*), which has led to the development of design guidelines per the American Concrete Institute (*8*) and the International Tunneling and Underground Space Association (*9*). The use of FEA is also recommended as an acceptable approach by ACI 544.7R-16 for determination of service state load conditions (*2*).

To ensure the durability of the tunnel during its operational life, PCTL segments are designed to incur minimal damage during installation. The segments and load pads are therefore sized to eliminate the potential for tensile crack formation. As a result of the thrust force, tensile stresses are expected to form in three general regions of the segment, as shown in Figure 1: (1) between the load pads (leading to transverse spalling stress), (2) under the load pads in the circumferential direction (due to transverse bursting stress), and (3) within the body of the segment under the load pads in the radial direction (due to radial bursting stress). Transverse bursting cracks can develop through the segment thickness and are usually observable on either the intrados or extrados surface of the segment. Radial bursting cracks are expected to form within the segment and therefore cannot be visually identified during construction or service.

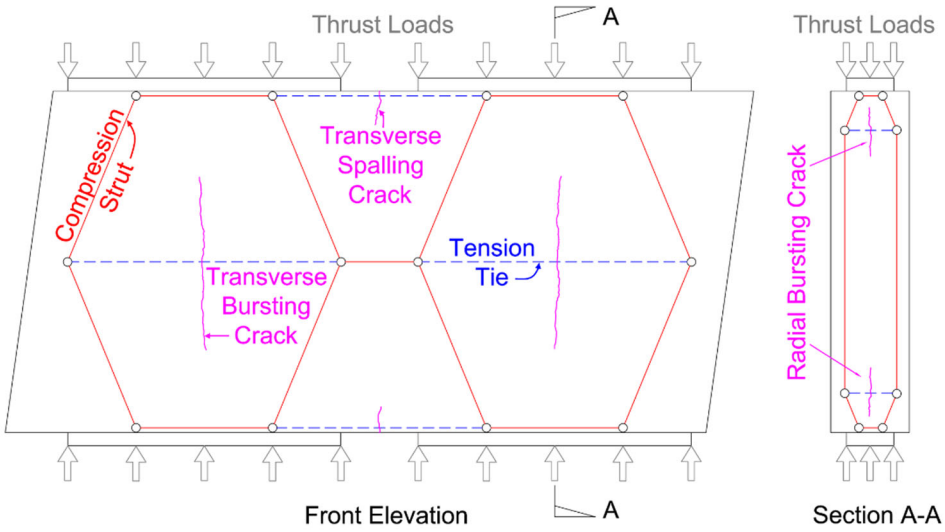

Figure 1: Simplified load transfer and potential crack formation in representative PCTL segment (note that compression struts and tension ties are for illustration and do not necessarily correspond to reinforcement locations).

Serviceability performance limits for PCTL segments under thrust jack loading are often tied to the formation and magnitude of cracks in the segment. The AASHTO LRFD Road Tunnel Design and Construction Guide specifies that crack widths shall be less than or equal to 0.2 mm (0.008 in.) to meet serviceability requirements of tunnel structures (*10*). Since most segment geometries are sized to prevent crack formation under maximum expected thrust forces, ultimate strength limit states are therefore rarely a design objective for those loads. To minimize crack size and limit crack propagation, fiber reinforced concrete (FRC) has been widely adopted for tunnel liners. Steel fiber reinforced concrete (SFRC) has emerged as one of the most common structural materials for tunnel segment fabrication in current practice (*11*). For example, Liao et al. (*12*) found that among 35 tunnel projects from 1982 to 2011, only five projects utilized conventionally reinforced concrete (RC) with steel bars and/or wire mesh. By eliminating the needs for the installation of conventional steel reinforcing bars prior to concrete placement, SFRC segments can significantly reduce fabrication time, material usage, and labor costs while still providing adequate strength and stiffness to meet all structural requirements (*3*, *13*, *14*).

Several previous studies (*13*, *15*, *16*) has demonstrated that PCTL segments constructed from SFRC and RC can provide similar performance under thrust jack load; however, testing has shown that SFRC exhibits smaller distributed cracks while an RC segment typically develops fewer larger crack (*17*), which is undesirable from a water penetration perspective. Additional studies have shown that the addition of polypropylene fibers (PP) to a segment with conventional steel reinforcement can also produce a more distributed formation of smaller cracks (and thus better residual serviceability) after being subjected to relatively high thrust jack load levels (*11*, *18*, *19*). To date, however, none of the available literature has examined the addition of steel fibers to a conventionally reinforced PCTL segment.

When the centerline of the thrust jack pads are not aligned with that of the bearing surface of the segment's circumferential joint, the resulting eccentricity can increase the transverse stresses and crack formation at a given thrust jack load. Previous numerical studies have shown that such an eccentricity in the segment's radial direction can cause crack formation at lower thrust jack load

and ultimately produce larger crack sizes (*20–23*). ACI 544.7R-16 therefore suggests that the potential eccentricity of the thrust jack load in radial direction should be considered in design. If no specific value has been provided for the particular TBM system, a generic 30-mm radial eccentricity should be considered in both the intrados and extrados directions (*2*). The impact of these eccentricities on realistically curved PCTL segments has not yet been evaluated in large scale experiments.

For this experimentation, six tests were performed to apply thrust jack load on full-scale PCTL SFRC segments used for a U.S. roadway tunnel. Double-pad load tests were performed to simulate the loading conditions used during TBM tunnel construction, and single-pad load tests were performed to evaluate the ultimate capacity of the segments. The thrust jack load magnitudes applied in these tests (up to 22.2 MN for a single pad thrust jack load) is significantly higher than that used in past experimental programs, which commonly ranged from only 1.1 MN to a maximum of 9.3 MN (*13*, *17*). The results of testing are evaluated against the aforementioned AASHTO service crack size criterion of 0.2 mm as well as numerical predictions from pre-test FE analysis. The goals of this chapter are as follows:

- Examine the development of tensile strains and the modes of cracking due to the increase of thrust jack loading (applied both concentrically and eccentrically in the radial direction) for the baseline SFRC segment design.
- Evaluate the influence of supplementary steel reinforcing bars, which when combined with the SFRC comprises a “hybrid” segment design.
- Demonstrate the design value of the “blind” FE analysis, particularly those with simpler linear material relationships, in predicting residual serviceability limits (i.e. to identify the governing modes and thresholds of cracking) for thrust jack loading on SFRC segments.

2.2. Precast Segment Properties

The baseline SFRC specimens for the study of segmental tunnel lining systems were obtained from a precast fabricator as duplicates segments for a tunnel liner currently under construction in the U.S. The hybrid segments which also included supplemental steel reinforcing bars were specially fabricated for this project using the same overall geometry and SFRC mix design. The tunnel is approximately 1.6 km in length, with an external diameter of 12.8 m, an internal diameter of 11.9 m, and resulting wall thickness of 457 mm. The tunnel consists of approximately 900 PCTL rings along its longitudinal direction, with each ring consisting of ten circumferential segments. Segments in this study have an 8° longitudinal joint skew to facilitate the tunnel’s longitudinal alignment, as shown in Figure 3. Each ring assembly consists of ten segments, including eight curved parallelogram segments, one large curved trapezoidal segment, and one curved trapezoidal key segment (highlighted in red). The segment lengths in the longitudinal tunnel direction range

from 1.93 m to 2.03 m, and widths in the circumferential direction are approximately 4.09 m for the larger segments and 1.96 m for the key segments.

The TBM thrust jack loads are applied at nineteen thrust pad locations distributed around the circumference of the tunnel as shown in Figure 2 and Figure 3. The nine larger segments are subjected to two thrust jack pad loads, and the smaller keys segment is only subjected to one. The segments are detailed to ensure linear force transfer along the longitudinal direction of the tunnel. This is accomplished with the addition of a 4.0-mm raised region on the front and rear circumferential joint of each segment as shown in Figure 2 and Figure 3. The load from the thrust jack pad is transmitted linearly to the preceding ring segments along the longitudinal direction of the tunnel. The rotational offset of each ring is arranged so the elevated portion of the previous ring aligns with the line of force from the thrust jacks as illustrated in Figure 3.

Thrust jack load is applied to each pad by two hydraulic jacks, which together can apply a maximum force of 9.55 MN per pad (referred to herein as the "maximum jacking capacity"). Based on the geotechnical profile for this particular tunnel alignment, the expected maximum thrust demand from the TBM during construction is 5.78 MN per pad, or 11.60 MN for each segment with two pads. Note that the maximum expected thrust jack load and the maximum jacking capacity load levels are used in the experimental program as key observation points to assess performance.

The hydraulic jack forces are distributed to the segment through a 120-mm thick steel plate and a 30-mm thick polytetrafluoroethylene (PTFE) pad, inserted between the steel plate and the concrete to reduce the development of localized lateral shear stress. The thrust jack pads are curved to align with the tunnel circumference and are dimensioned to be 1600-mm long by 276-mm wide (see Figure 2 and Figure 3). The centerline of the hydraulic jacks and the centerline of the concrete segment are concentric. The contact area, however, is radially offset by 4.8 mm toward the intrados surface due to the presence of a waterproofing gasket near the extrados surface as shown in Figure 2.

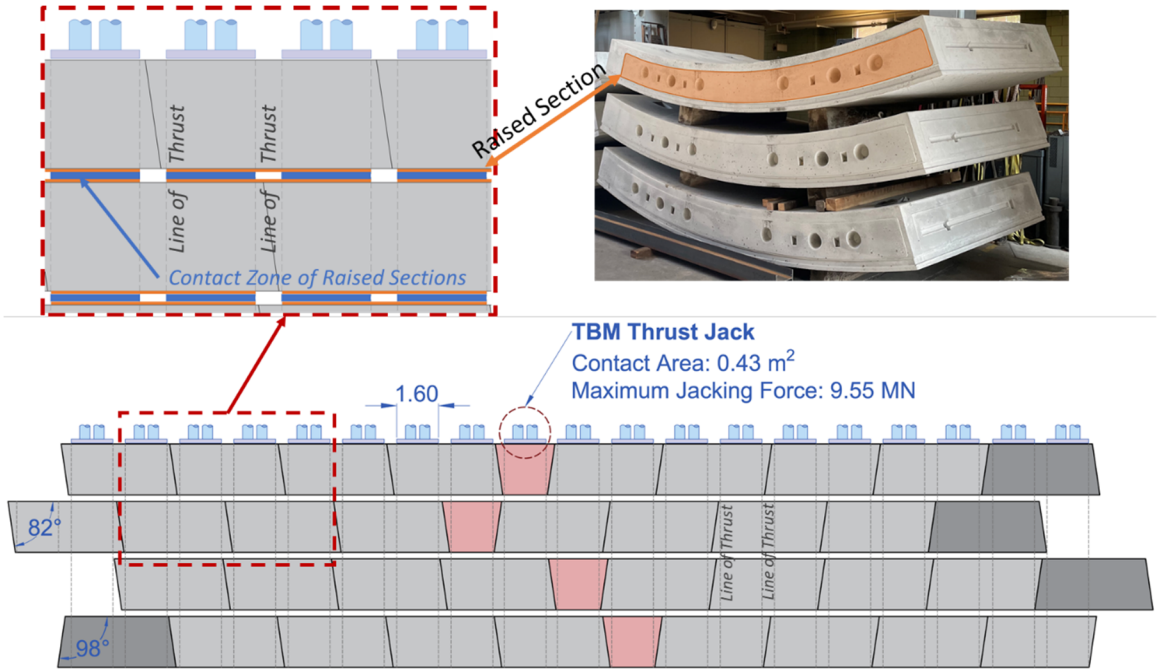

Figure 2: Illustration of lining segments and ring configuration (shown unwrapped) for the prototype tunnel (units: m)

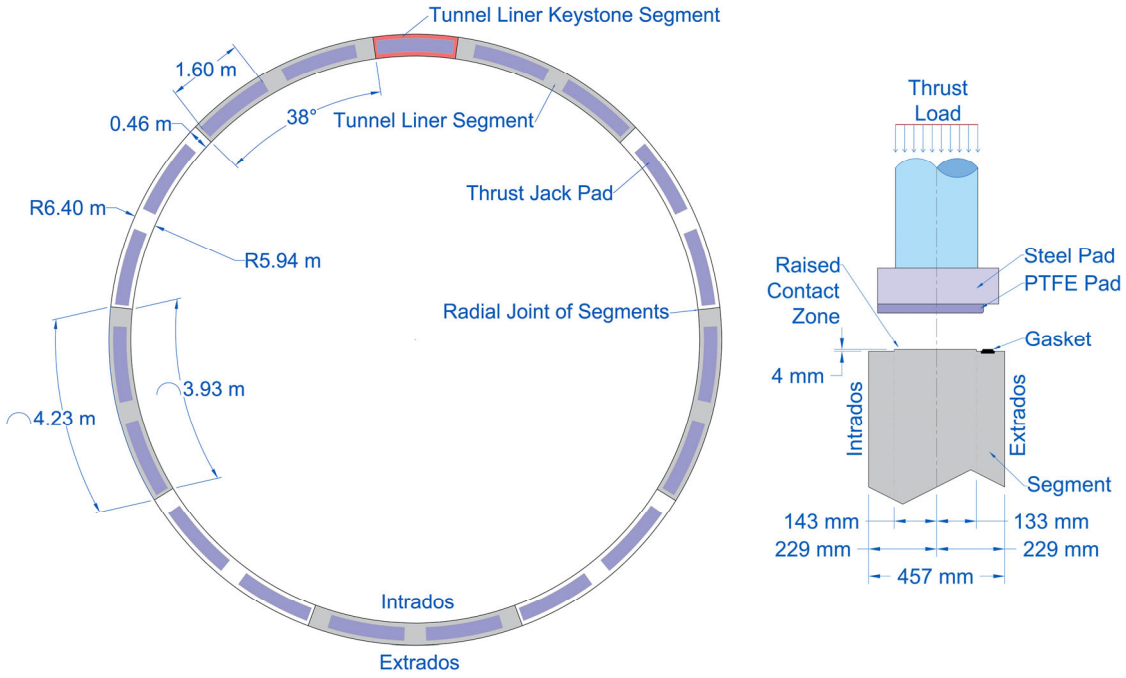

Figure 3: Illustration of TBM thrust jacking loads applied to ring bearing area

2.2.1. Steel Fiber Reinforced Concrete Properties

All segments for the tunnel project and the specimens in this study utilize an SFRC mix which was designed to provide not only the requisite compressive strength but also enough tensile strength to

enable the elimination of conventional reinforcing bars. Table 1 summarizes the mix proportions as well as the plastic properties from a typical sample. The mix utilizes Type I/II Portland cement with the following replacements by weight: 40% slag replacement and 5% silica fume. Dramix 4D steel fibers, which conform to ASTM A820, EN 14889-1 and ISO Class A (*24–26*), were added at 0.510% by volume. Each fiber has a length of 60 mm and a diameter of 0.75 mm, and both ends are crinkled for enhanced bond with the concrete. Each fiber is composed of cold drawn steel wire has a nominal tensile strength of 1800 MPa, an elastic modulus of 200 GPa, and an ultimate strain of 0.8%.

Table 1: SFRC mix design

Constituent	Description	Values
Cementitious	Cement I/II	243.2 kg/m^3
	Grade 120 GBFS (Granulated Blast Furnace Slag)	178.0 kg/m^3
	Sikacrete 950 DP Silica Fume	23.7 kg/m^3
	Total Cementitious	445.0 kg/m^3
Aggregate	Coarse Aggregate #8	949.2 kg/m^3
	Fine Aggregate	688.2 kg/m^3
Steel Fiber	Dramix 4D Fiber	38.6 kg/m^3
Water	Water	155.7 kg/m^3
	Water/Cement Ratio	0.350
Design Air	Entrained	6.0%
Superplasticizer	Sika ViscoCrete 6100	4.7 kg/m
Air Entraining Admixture	Sika AEA 14	0.8 kg/m^3
Sample Measured Plastic Properties	Slump	2544 mm
	Air Content	5.5%
	Concrete Temperature	20.0 °C
	Ambient Temperature	19.4 °C
	Unit Weight	2337 kg/m^3

The SFRC compressive strength and elastic modulus were assessed in accordance with ASTM C39 and C469 (*27*, *28*), respectively. Uniaxial tensile properties can be determined using inverse analysis of small-scale flexural beam test results (*2*) or through a direct tension test approach (*29*). For the SFRC mix in this study, splitting tensile strength and the crack mouth opening displacement (CMOD) were determined in accordance with ASTM C496 and EN 14561 (*30*, *31*), respectively. Table 2 summarizes the properties measured by the precast fabricator when the specimens were cast as well as those measured by the research team prior to thrust jack load. A total of 12 CMOD tests conducted by the precast fabricator are plotted in Figure 4(a), in which the average curve is represented as a single thick black line. As shown in Table 2, all properties met the required minimum values for the design of these segments.

Table 2: SFRC structural material properties

Property	Required Min. Value [MPa]	Fabricator Measured Value [MPa] (age in days)	Measured from Cores [MPa] (age in days)
Elastic Modulus	34000 short term 20000 long term	Not available	30940+/-1550 (610 to 723)
Poisson's Ratio	Not Specified	Not Available	0.196+/-0.02171

Compressive Strength	52	65.6+/-5.2 (28)	64.3+/-9.5 (610 to 723)
Splitting Tensile Strength	4.2	7.34+/-0.17 (28)	7.05+/-0.85 (610 to 709)
CMOD Peak Strength	4.2	7.12+/-0.32	Not Applicable
CMOD 0.5 mm	Not Specified	4.57+/-0.83	Not Applicable
CMOD 1.1 mm	4.82	5.83+/-1.32	Not Applicable
CMOD 3.5 mm	3.45	6.28+/-1.30	Not Applicable

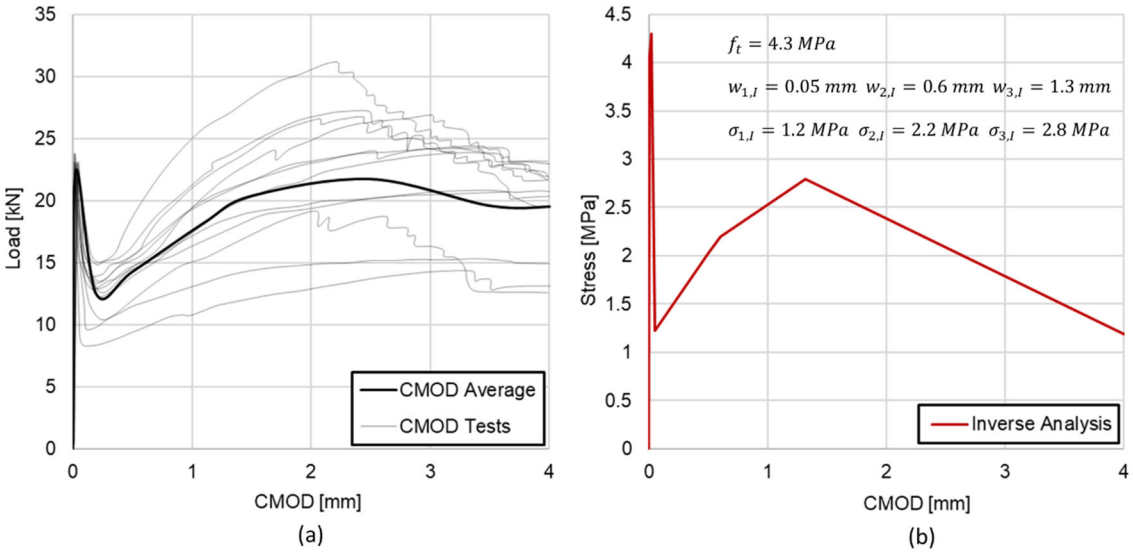

Figure 4: CMOD test data: (a) measured load-displacement, and (b) inverse analysis results to obtain stress-displacement

The resistance of the segments to thrust jack loading was assessed relative to the formation of cracks in the SFRC material (which were measured via strain gauges and visual inspection during and after each test). The strain at cracking is calculated by dividing the tensile strength by the measured average elastic modulus noted in Table 2. Uniaxial tensile strength can be estimated using three approaches, the results of which would be expected to bound the actual cracking strain in the segments. The first approach calculates the tension strain limit using the measured split cylinder tension strength. The loading condition for a split cylinder test does not generate a uniform tension stress profile, the this approach is therefore considered to provide only an approximate upper bound estimate (*32*, *33*). The two other approaches, described below, consist of an inverse analysis of the CMOD data (*34*) and an additional approach proposed by RILEM (*35*) and recommended by ACI (*8*).

The second approach consists of an inverse analysis of the CMOD data (*34*). Specifically, the approach is based on a closed-form solution that relates the multi-linear stress-crack opening to the load-CMOD curve. A tetralinear model of the stress-crack opening curve was computed as shown in Figure 4b. The analytical model is based on the concept of a non-linear hinge formation in a three-point bending test (*36*). The nonlinear hinge is placed at midspan with length equal to half the beam depth. The hinge is modeled as layers of spring elements with their behavior governed by the tensile constitutive relation of the concrete. The parameters of the SFRC stress-crack width curve were found by fitting the CMOD curve obtained from EN14651 tests (*31*) on the SFRC (Figure 4b). The solid black line shows the load-CMOD curve using the average values

of inverted parameters from individual tests, and the red line shows the stress-crack width relationship using the average inverse parameters. An average peak tensile strength, f_t, of 4.3 MPa is estimated via the inverse analysis. The estimated average residual tensile strengths, $\sigma_{i,I}$, corresponding to crack widths, $w_{i,I}$, of 0.05, 0.6, and 1.3 mm are 1.2, 2.2, and 2.8 MPa, respectively. The strain values at these crack openings are large and should not be used as a limit state for the serviceability check.

The third approach, proposed by RILEM (*35*) and recommended by ACI (*8*), suggests that the residual flexural strength corresponding to a crack mouth opening of 0.5 mm should be used to determine the serviceability limit state. The approach converts the measured flexural tensile strength of an SFRC beam to a uniaxial tensile strength using Equation 1:

$$f_t = C_1(1.6 - d)f_{tm,fl} \quad \text{Equation 1}$$

where d is the depth of the beam's cross-section, and $f_{tm,fl}$ is the average value of the measured peak flexural tensile strength before cracking (7.12 MPa). C_1 is assumed to be 0.52 (*37*), and the resulting estimated uniaxial tensile strength is therefore 5.46 MPa. The uniaxial residual strength, $f_{t,r}$, and corresponding strain, $\varepsilon_{t,r}$, at 0.5 mm crack mouth opening can then be expressed according to equations 2 and 3.

$$f_{t,r} = 0.45 \cdot f_{R,1} \cdot \kappa_h \quad \text{Equation 2}$$

$$\varepsilon_{t,r} = \frac{f_t}{E_c} + 0.001 \quad \text{Equation 3}$$

where $f_{R,1}$ is the 0.5 mm post-crack residual flexural strength (4.57 MPa); E_c is the elastic modulus of SFRC; and κ_h is the size factor of the specimens used for beam flexural tests (equal to 1 for a beam specimen with 150-mm depth and a 25-mm deep notch at the tension face).

As summarized in Table 3, the uniaxial tension strain limit ranges from 139 to 237 $\mu\varepsilon$, with the lower bound from the inverse analysis approach and the upper bound from the split cylinder data. This range from the lower limit, $\varepsilon_{t,l}$, to upper limit, $\varepsilon_{t,u}$, will be used as the basis for evaluating the strain data acquired from thrust jack load testing of the full-scale segments. The strain at 0.5 mm post-crack residual uniaxial strength is computed from the inverse analysis to be 6667 $\mu\varepsilon$. A strain of 1066 $\mu\varepsilon$ at the 0.5 mm post crack displacement is determined using the RILEM approach and is calculated using Equation 3.

Table 3: Tensile stress and strain limits of SFRC

Approach	Strength Type	Stress Limit (MPa)	Strain Limit ($\mu\varepsilon$)
Splitting Tension Tests	Splitting Tensile Strength, $f_{t,sp}$	7.34	237
CMOD Tests	Flexural Tensile Strength, $f_{tm,fl}$	7.12	230
	0.5 mm Post-Crack Residual Flexural Strength, $f_{R,1}$	4.57	N.A.
Inverse Analysis	Uniaxial Tensile Strength, $f_{t,i}$	4.30	139
	0.5 mm Post-Crack Residual Uniaxial Strength, $f_{t,r,i}$	2.03	6667
RILEM Approach	Uniaxial Tensile Strength, f_t	5.46	176
	0.5 mm Post-Crack Residual Uniaxial Strength, $f_{t,r}$	2.06	1066

2.2.2. Conventional Reinforcement for Hybrid Segments

The performance of the baseline SFRC segments is compared against that of hybrid segments for which carbon steel reinforcing bars are used in conjunction with the same SFRC mix. As shown in Figure 5, two rows of longitudinal bars are installed parallel to each joint face, and radial tie-bars are included to provide confinement against bursting in the radial direction at these locations (thus forming a ladder pattern with longitudinal bars). All bars confirm to ASTM A615 Grade 420 (*38*) and have a standard cover of 50.8 mm per ACI 318 for reinforced concrete elements exposed to weather (*39*). All contact points between bars are welded to ensure full development due to limits space within the segment. Tensile testing on samples of the No. 19, 22, and 25 reinforcing bars that were used in the hybrid specimens produced an average yield strength of 412.5, 415.0 and 451.0 MPa, and average tensile strengths of 627.6, 585.9, and 643.7 MPa, respectively.

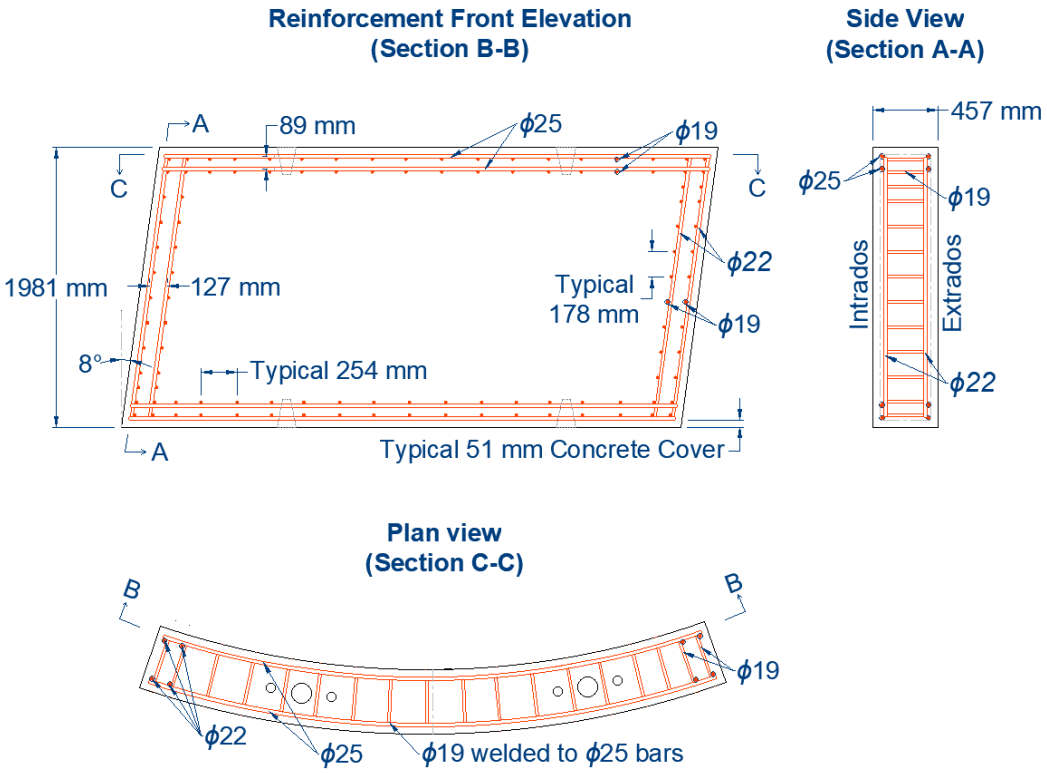

Figure 5: Layout and detailing for steel reinforcing bars in the hybrid segments

2.2.3. Numerical Predictions of Expected Thrust jack load Response

Four 3D FE models were developed using Abaqus CAE/Standard (*40*) to calculate the expected response of the PCTL segment specimens to thrust jack loading. All models use the measured value of elastic modulus (30,940 MPa per Table 2) as direct input. Model 1 has an elastic SFRC material model with thrust jack load applied in a concentric manner per Figure 3 (i.e. without eccentricity). Models 3 and 4 are duplicates of Model 1 but with the thrust jack load applied at an eccentricity of 51 mm towards the intrados and extrados surfaces, respectively. The 51-mm eccentricity value was recommended by the TBM manufacturer for the segments in this study and is larger than the standard 30-mm value recommended by ACI 544-7R (*2*).

Model 2 utilizes the same concentric thrust jack load as Model 1 but utilizes a nonlinear concrete damage plasticity (CDP) material model for the SFRC, based on the measured material properties and *fib* MC-2010 (*14*). The measured value of compressive strength (65.6 MPa) and the uniaxial tension properties from inverse analysis of the CMOD test data were used as input for the nonlinear material in Model 2. The resulting constitutive stress-strain relationships for SFR in Model 2 are plotted in Figure 6.

Table 4: Matrix of FE models used to predict the expected response of a single SFRC segment to thrust jack loading

Model No.	SFRC Material Model	Thrust jack load Application
1	Linear Elastic	Double Pad, Concentric
2	Nonlinear (see Figure 6)	Double Pad, Concentric
3	Linear Elastic	Double Pad, Eccentric at 51 mm towards Intrados

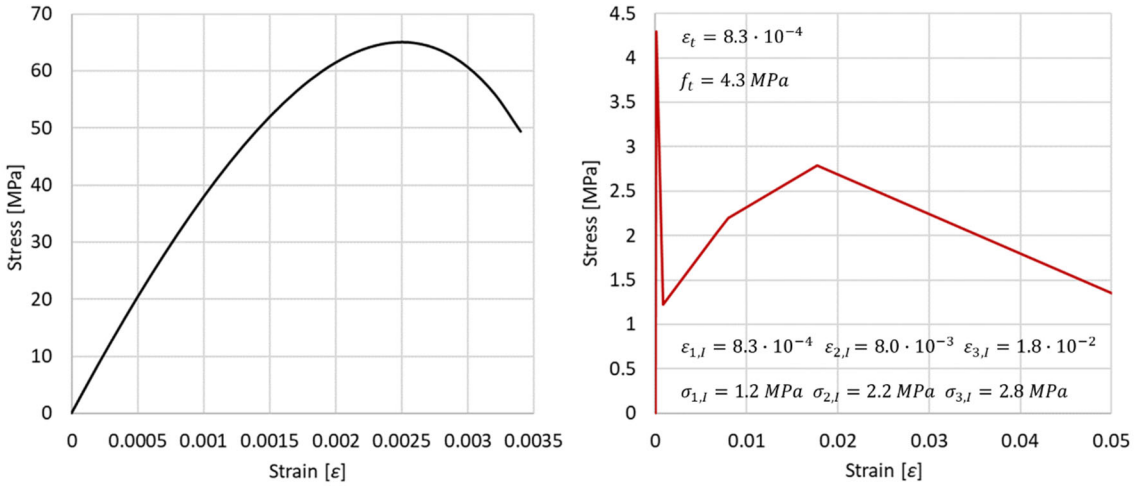

Figure 6: Nonlinear stress-strain relationships (left: compression, right: tension) used as input for Model 2

The FE model uses C3D8R (reduced integration) solid elements with an average mesh size of 38 mm (as determined via a preliminary convergence study). The red-highlighted areas at the bottom of the segment in Figure 7 are vertically (i.e. longitudinally) restrained and have additional restraints in the horizontal plane that are marked with red triangles. The horizontal restraints were needed to maintain static equilibrium amd were applied in such a pattern as to not artificially over-restrain the supported faces. As shown in Figure 7, the thrust jack load application is idealized as a uniform pressure over the thrust jack pads per their footprint in Figure 2. To evaluate the impact of this simplification, a preliminary analysis of Model 1 was also conducted in which a 30-mm thick Teflon pad (used by the actual TBM thrust jacks) was placed on top of the highlighted loading zones in Figure 7 and then loaded with the same uniform pressure. The results of that analysis showed no substantial difference in stress distributions versus the simplified case with direct load application (which was therefore used for all subsequent analyses).

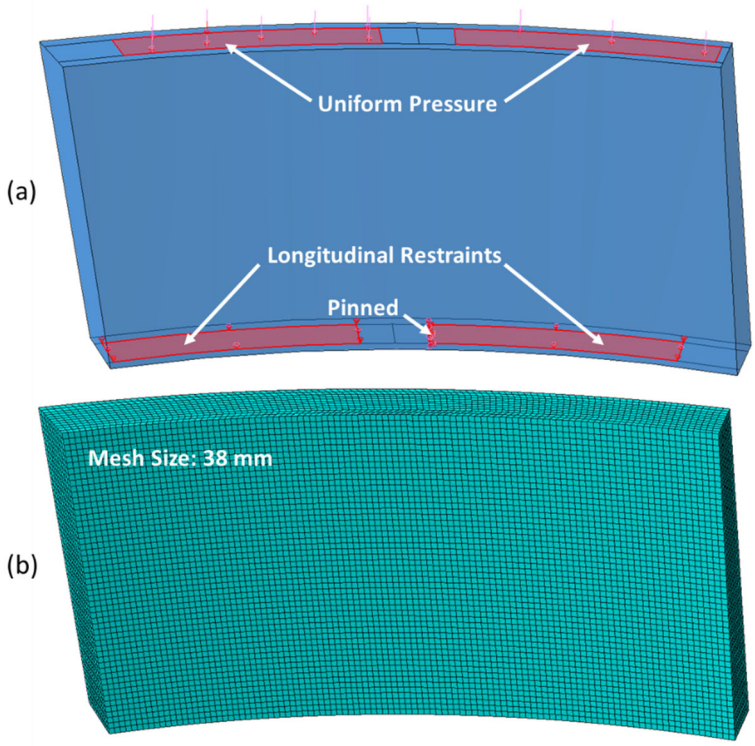

Figure 7: FE model setup: (a) loading and boundary conditions, and (b) mesh

The maximum principal strain contours from Model 1 with 7.4 MN applied to each pad are plotted in Figure 8, as well as the general locations where bursting and spalling tensile strains are developed due to thrust jack load. The observed regions of elevated tensile strain correlate with the expected damage zones illustrated in Figure 1. The cross-section at the white dashed line in Figure 8 illustrates the radial bursting strain distribution within the segment thickness under the center of a load pad. The maximum transverse spalling strain forms between the load pads in the transverse (i.e. circumferential) direction. The maximum transverse bursting strain develops at the mid-width of the segment under the load pad, again along the transverse direction. The maximum radial bursting strain develops near the load pad at approximately 200 mm (less than half the segment thickness) under the highlighted loading zone along the radial (i.e. thickness) direction. The maximum principal strain contours from Model 2 with 7.4 MN at each load pad are very similar to those shown for Model 1 in Figure 8 and are therefore not plotted for brevity.

The results of Model 3 are plotted in Figure 9; as expected, radial eccentricity toward the intrados causes global flexure and an increase in compression, which increases the transverse bursting strain on the intrados face. Similarly, eccentricity toward the extrados for Model 4 in Figure 10 decreases the strain in that area. The eccentricity also affects the distribution of transverse spalling strains, which marginally increase on the bearing side (i.e. bottom circumferential joint) for the intrados eccentricity and significantly increase on the loading side (i.e. top circumferential joint) for the extrados eccentricity. As would be expected, these results indicate that an eccentric thrust jack load application would likely result in earlier formation of transverse spalling cracks versus a concentric load.

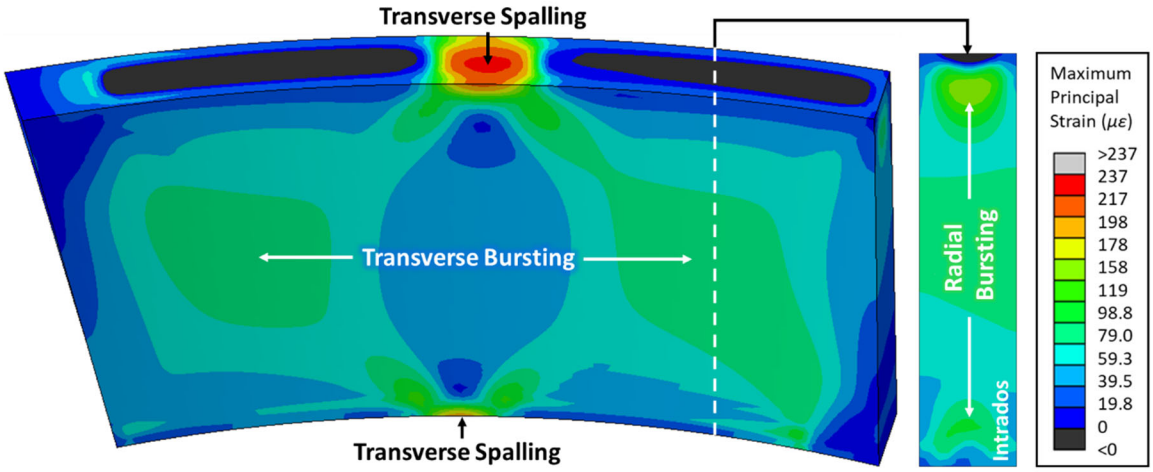

Figure 8: Maximum principal strain of Model 1 under 7.4 MN per pad

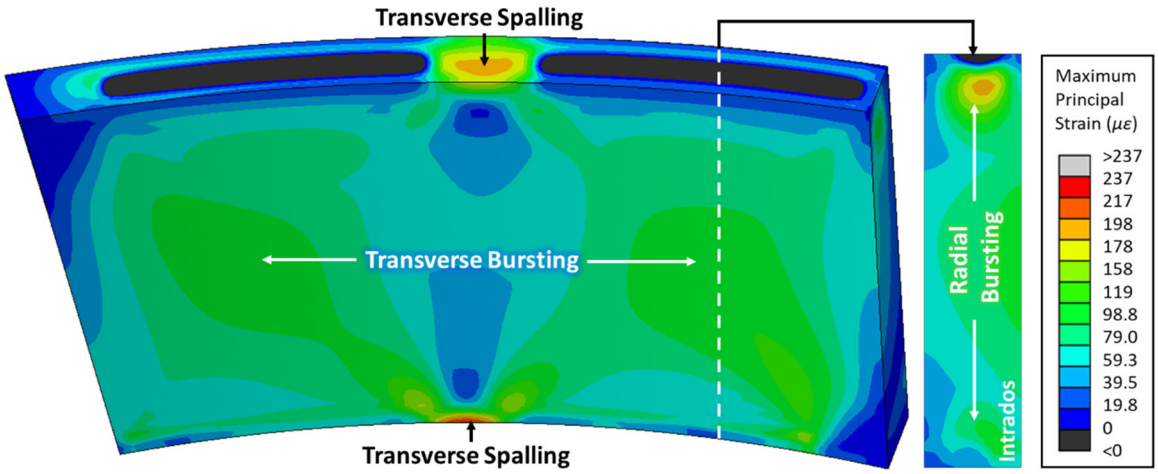

Figure 9: Maximum principal strain of Model 3 (51 mm intrados eccentricity) under 7.4 MN per pad

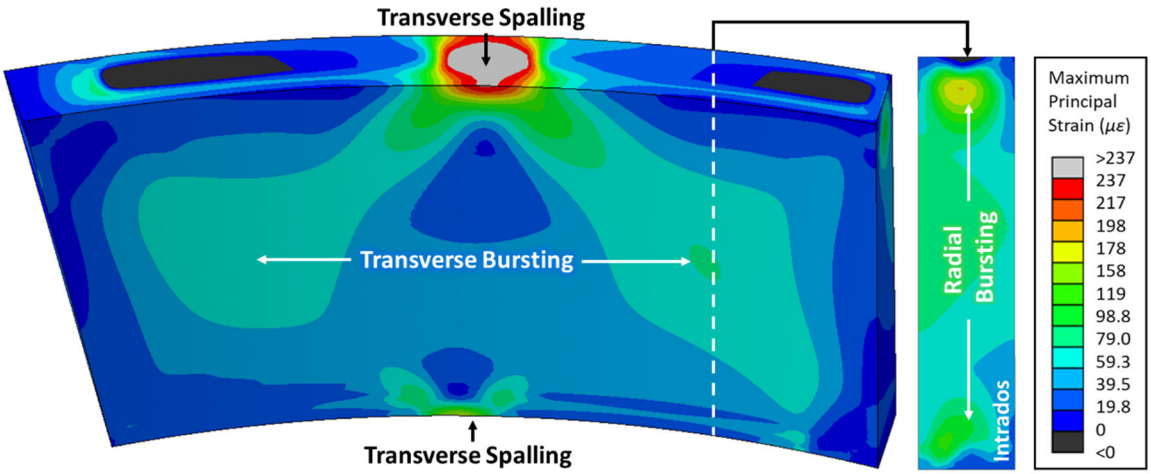

Figure 10: Maximum principal strain of Model 4 (51 mm extrados eccentricity) under 7.4 MN per pad

Tensile strain output from the FE models are used to determine the expected load level and the corresponding locations at which the segment would develop tensile cracking (compared against the lower and upper bound limits, $\varepsilon_{t,l}$ and $\varepsilon_{t,u}$, of 139 and 237 $\mu\varepsilon$ per Chapter 2.1). Since Models 1, 3 and 4 are elastic, it should be noted that the simulated tensile stress-strain response is not impacted by those limits and can continue to increase past the point at which a crack would realistically. Therefore, any results produced after the tensile limit is first reached at any location in the elastic model can accumulate error if the crack formation impacts the subsequent stress flow at escalating load levels. The results of elastic Model 1 at progressive states of cracking are therefore compared against those from the inelastic Model 2 to examine the impact of crack-induced tensile stress limitations on stress flow within the segment.

Table 5: Total thrust jack load per pad (MN) corresponding to tensile strain limits for each cracking mode in Figure 1

Case	Transverse Spalling		Radial Bursting		Transverse Bursting	
	$\varepsilon_{t,l}$	$\varepsilon_{t,u}$	$\varepsilon_{t,l}$	$\varepsilon_{t,u}$	$\varepsilon_{t,l}$	$\varepsilon_{t,u}$
Model 1	4.7	7.8	6.8	11.3	10.6	18.0
Model 2	4.7	N.A.	6.6	N.A.	10.6	N.A.
Model 3	4.2	7.3	5.4	9.3	8.9	15.6
Model 4	3.9	6.4	5.8	9.8	10.5	18.0

The total applied thrust forces needed to reach the tensile limits due to transverse spalling, transverse bursting, and radial bursting are summarized in Table 5. Transverse spalling cracks occur first for all models, followed by radial bursting and then by transverse bursting. Recall that the inelastic Model 2 uses the concrete tensile constitutive properties defined in Figure 6, which is based on the lower bound tensile strain limit, $\varepsilon_{t,l}$. Consequently, no upper bound values are reported for Model 2. Therefore, the comparison that follows between all four models is predicated on the results in Table 5 for $\varepsilon_{t,l}$. Thrust pad loads corresponding to the upper bound tensile strain limit, $\varepsilon_{t,u}$, are provided in Table 5 to establish an upper bound threshold against which the results of testing will be evaluated later in Chapter 4.

Results for Models 1 and 2 in Table 5 both indicate the first instance of cracking via transverse spalling per $\varepsilon_{t,l}$ at the same 4.7-MN thrust pad load. This result confirms the negligible influence

of material nonlinearity at this load level. As the thrust jack load subsequently increases, the models continue to produce very similar results. Specifically, radial bursting per $\varepsilon_{t,l}$ is reached only 3% sooner in the inelastic Model 2, and both models reach transverse bursting per $\varepsilon_{t,l}$ at the same 10.6-MN load. These results indicate that tensile cracking had a nearly negligible impact on the stress flow in these segments, which have substantial size and can widely distribute stresses throughout the SFRC material around cracks. The SFRC material acts more like a continuum for tensile stress redistribution, as opposed to a conventionally reinforced segment without fibers which relies on its reinforcing bars to discretely resist post-cracking tension forces. The linear FE model can therefore provide a suitably accurate prediction of the location and thrust jack load at which tensile cracking occurs in these SFRC PCTL segments.

As would be expected, results for Models 3 and 4 in Table 5 show that progressive tensile cracking at all three modes is reached at slightly lower thrust pad loads compared to Model 1 due to the additional flexural and arching stresses induced by eccentric loading. Transverse spalling is more heavily impacted by the extrados eccentricity, as Model 4 needs 17% less thrust jack load to reach this mode of tensile cracking per $\varepsilon_{t,l}$ than Model 1. Both radial and transverse bursting are more impacted by the intrados eccentricity in Model 3, again at ~17% less thrust jack load for both modes compared to Model 1. These results suggest that an expected upper bound thrust jack load eccentricity should be accounted for when linear FE models are used to design this type of PCTL segment.

2.3. Experimental Program

2.3.1. Specimen Matrix

Six experiments, summarized in Table 6, were conducted on individual PCTL segments per the schematic in Figure 11, which reasonably emulated thrust jacking load from a TBM: three double pad tests and three single pad tests. A universal testing machine with 22.2-MN capacity was used to apply quasi-static loading at a rate of 0.300 MN/min, and loading was paused at multiple levels to observe and record crack formation. Cracking patterns and sizes were marked progressively through the loading history and documented. The double pad load tests were performed first and represented a conventional thrust jack loading condition with concentric load positioning. The results of these tests enable a direct comparison between the SFRC and hybrid reinforced segments (see Figure 5).

As will be shown later in Chapter 4, these tests exhibited a similar progressive onset of tensile cracking as the FE model results in Table 5; however, none of the double pad tests were able to surpass their ultimate resistance (i.e. “fail” due to a rapid loss of stiffness) due to the load capacity of the testing machine, which could apply ~11.1 MN at each pad. Three additional tests were then performed with a single pad load, which is not representative of actual TBM installation process for these segments but could ensure that the ultimate load from a single pad would be reached. Two of the single pad tests used concentric loading, while the third used a 38-mm extrados eccentricity. Recall that the extrados eccentricity of Model 4 produced the earliest onset of the first tensile cracking via transverse spalling (see Table 5). The extrados direction for the third single pad test would therefore be expected to produce a conservative onset of the first instance of tensile cracking.

To emulate the TBM thrust jack pad load transfer, a 6.4-mm thick steel plate and a 3.2-mm thick PTFE sheet were sandwiched as a bearing pad between the spreader beam and the top of the concrete segment. At the bottom of the segment, a 6.4-mm thick steel shim was used to create a boundary condition similar to what would be provided by a preceding tunnel ring as shown in Figure 3. The dimensions of the steel pads and Teflon/PTFE sheets used in the experiment are shown in Figure 11. The physical arrangement of the loading system and segments within the universal testing machine are pictured in Figure 12.

The segments were procured from the actual tunnel construction effort and therefore considerably ranged in age when tested. As shown in Table 6, the segment age on the day of thrust jack load testing ranged from 199 to 673 days after casting; however, the compressive and tensile strengths of the concrete did not vary significantly from 28 to 709 days, as shown previously in Table 2. It should be noted that four total segments (two each for SFRC and hybrid) were tested in this program. One SFRC and two hybrid segments were used initially for double pad load tests – as will be discussed later in Chapter 4, these specimens only exhibited marginal observable tensile cracking when subjected to the 11.1-MN maximum pad load in this setup. The two hybrid segments were therefore reused for a second test under single pad loading to reach their ultimate response.

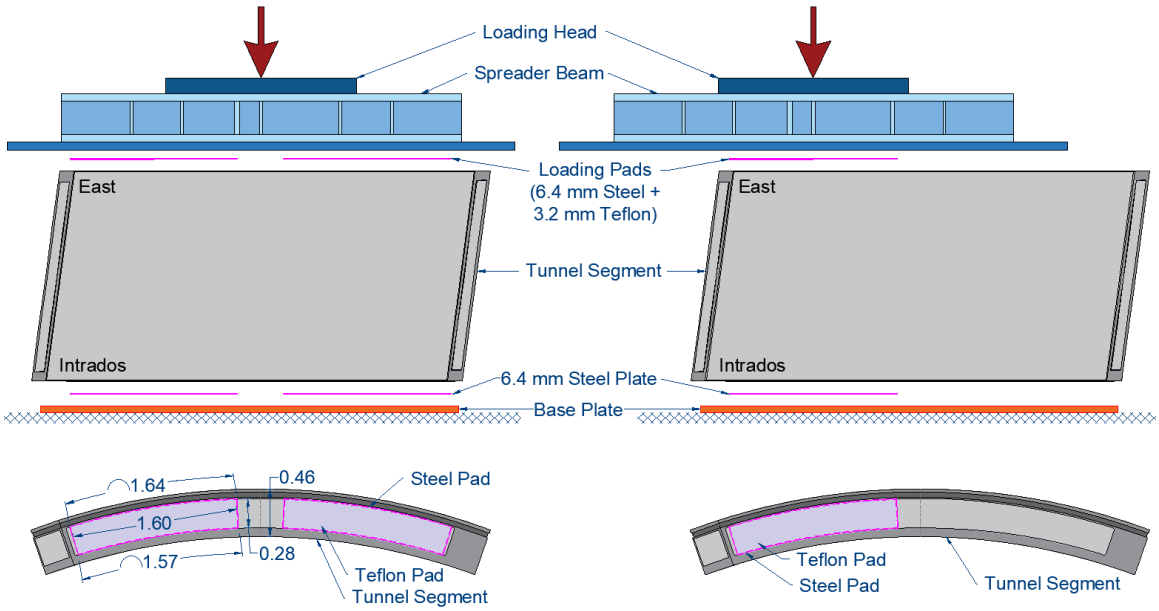

Figure 11: Configuration of double pad test (left) and single pad load test (right)

Table 6: Matrix of six thrust jack load tests, conducted on four total PCTL segments

Test ID	Type	Loading Condition	Age at Testing	Description
D-SC	SFRC	Double Pad, Concentric	673 days	Serviceability Test for SFRC
D-HC	Hybrid	Double Pad, Concentric	214 days	Serviceability Test for Hybrid Reinforcement
D-HC-2	Hybrid	Double Pad, Concentric	199 days	Duplicate of Test D-HC
S-SC	SFRC	Single Pad, Concentric	313 days	Ultimate Test for SFRC

S-HC	Hybrid	Single Pad, Concentric	203 days	Ultimate Capacity Test for Previously Tested D-HC-2 Specimen
S-HE	Hybrid	Single Pad, Eccentric	216 days	Ultimate Capacity Test for Previously Tested D-HC Specimen, with 38 mm Eccentricity to Extrados Surface

Figure 12: Test setups for thrust jacking load testing

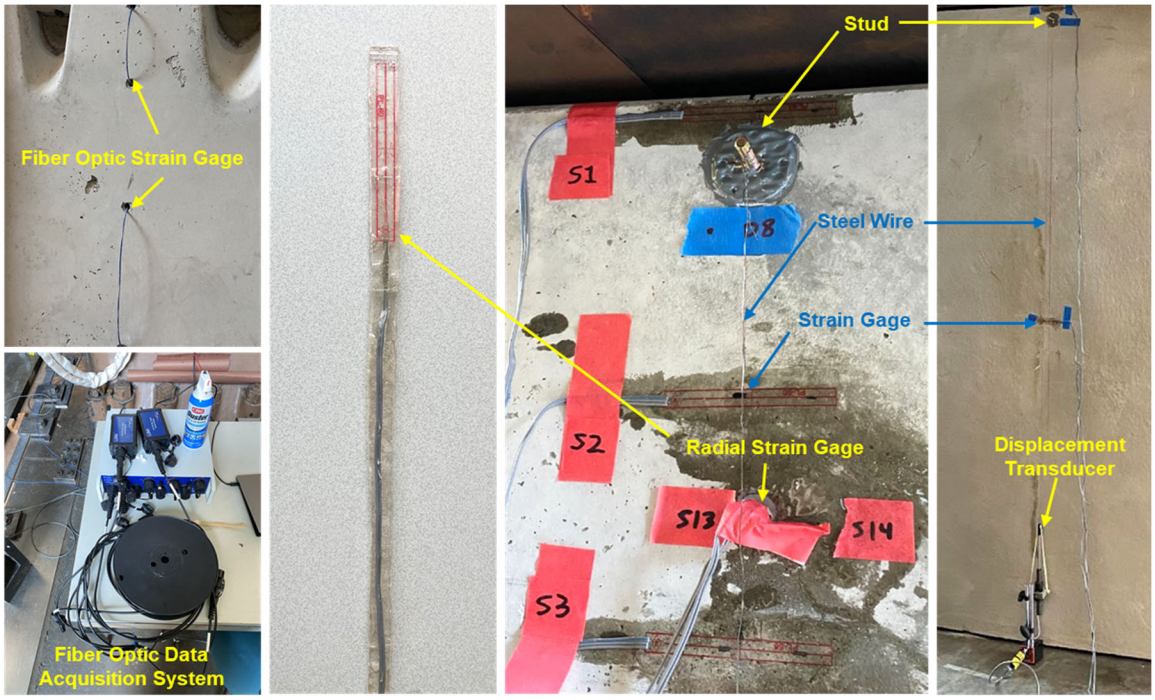

Figure 13: Segment instrumentation examples: fiber optic system, strain gage, radial strain gage, and displacement transducer

2.3.2. Instrumentation

All segments were instrumented with resistance-based strain gages and displacement transducers as shown in Figure 13. Displacement transducers were used to monitor the global position of the segment during loading. The strain gage layout (illustrated in Figure 14) was informed by the strain distribution results from FE models (see Figure 8) to target noteworthy regions of response. Transverse strains were measured using surface mounted resistance-based gages. For the D-SC specimen, a snaking strand of fiber optic strain gages was inserted through small holes which were then filled with hard epoxy to obtain a continuous measurement of radial strain through the segment thickness. For all other specimens, radial strains were measured using resistance-based gages placed into small predrilled holes (16-mm diameter). To facilitate their installation, these radial strain gages were first mounted onto epoxy sticks and then inserted into the predrilled holes. The holes were then filled with the same epoxy to achieve strain compatibility between the gage and the surrounding concrete. For verification, a preliminary uniaxial compression test was conducted on a concrete cylinder which was instrumented with this embedded strain gage on-a-stick as well as several surface bonded gages. The measured strains up to the onset of nonlinear behavior before crushing showed good agreement between the two methods.

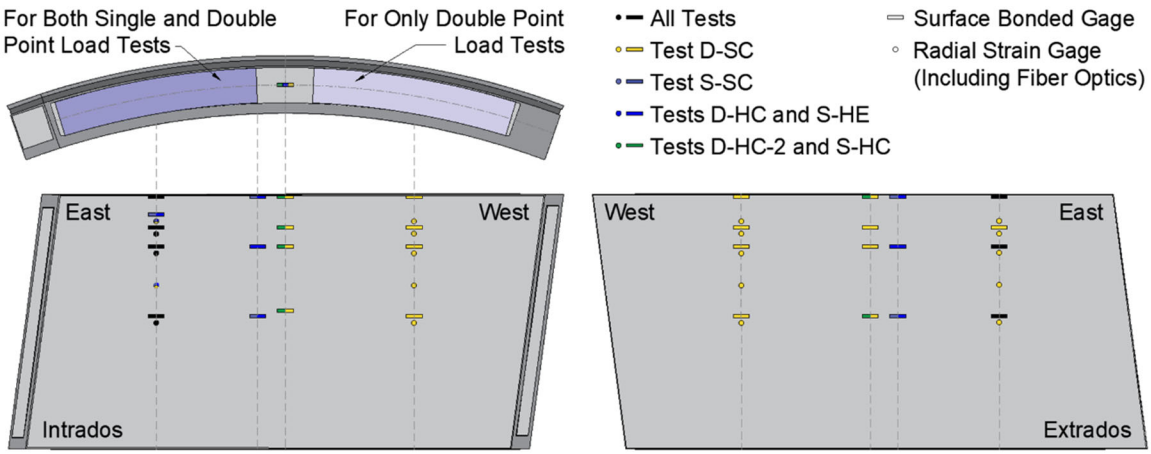

Figure 14: Strain gage layouts for all specimens

2.4. Results and Discussion

The thrust pad load-time histories of all six tests are plotted in Figure 15. The periodic stepwise pattern in these curves indicates a loading pause for crack observations. At pauses of loading, cracks were traced with a permanent marker and labeled with the load level. Maximum crack widths were measured using a standard crack comparator card. Loading continued until either the full 22.2-MN capacity of the universal testing machine was applied or ultimate failure of the segment occurred due to a rapid loss of axial resistance. Four tests (D-SC, D-HC, S-HC, and S-HE) were able to withstand the full 22.2-MN capacity of the testing machine without reaching ultimate failure. The double pad load test on the hybrid-reinforced segment (D-HC-2) was stopped at an applied force level of 10.0 MN per pad (10% short of the maximum pad load in this setup) to minimize damage accumulation and enable a subsequent single pad load test (S-HC). Only the single pad load test on the SFRC segment (S-SC) resulted in ultimate failure due to radial bursting prior to reaching the loading capacity of the testing machine.

The thrust jack load is also plotted in Figure 15 as a function of average displacement for each test, which represents the load-induced deformation from the top of the segment to the base plate (see Figure 11). For double pad tests, the displacement is averaged from the data collected by all four displacement transducers located on extrados and intrados faces under both loading pads (see Figure 13). For single pad tests, the displacement is averaged from the data collected by the two displacement transducers located on the extrados and intrados sides where thrust jack load is applied. The SFRC segment under double pad load (D-SC) exhibited higher stiffness in comparison with both tests on hybrid segments under the double pad load. This is likely attributed to the advanced age of 673 days (and associated curing gains in concrete stiffness) at testing, in comparison to the two hybrid segments which were aged 200 days at testing. The SFRC and hybrid segments under concentric single pad load exhibit similar trends in global load–deformation behavior. The hybrid segment under eccentric single pad loading (S-HE) exhibits a higher initial stiffness than the single pad concentric cases (S-HC and S-SC); however, the S-HE specimen softens at approximately 10 MN, after which its curve trends back to the other single pad specimens at higher loads.

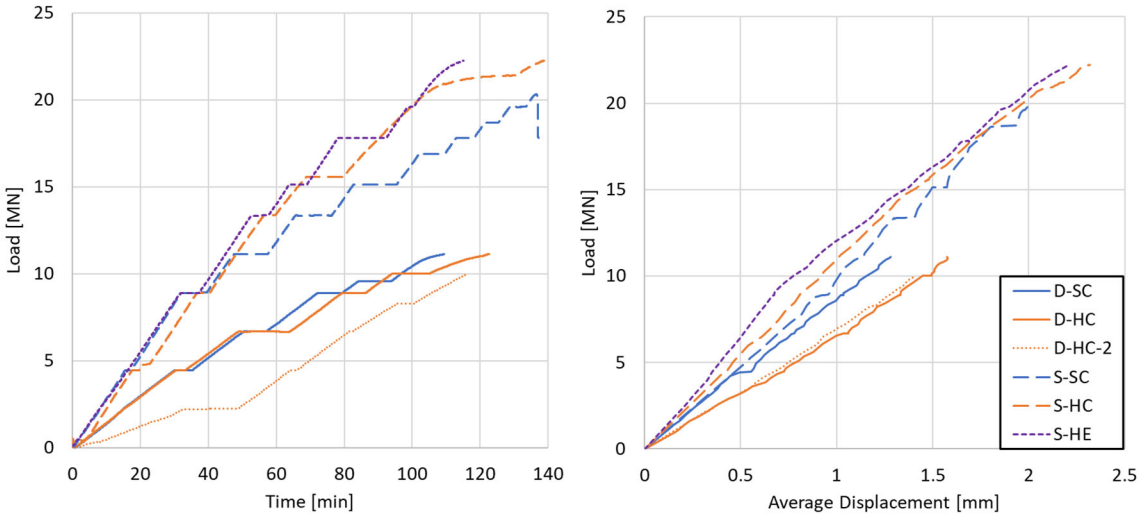

Figure 15: Thrust jack load histories for all tests: load per pad versus time (left), and load per pad versus average vertical displacement (right)

2.4.1. Serviceability Assessment (Double Pad Load Cases)

The performance of the segments under conventional double-pad thrust jack loading is assessed relative to the crack formation and strain measurements at the maximum expected thrust jack load during the construction of this particular tunnel (5.78 MN per pad) and at the maximum capacity of the TBM's jacking system (9.55 MN per pad). The crack markings on each specimen (made during the load stoppages in each test) were postprocessed to create a map of crack propagation with increasing load. Figure 16 presented a post-test, perspective-corrected crack propagation map for the intrados and extrados surfaces of each double pad loaded segment. Recall that crack widths were measured discretely at specific load levels; therefore, the lines between the pads do not represent crack growth but are used for illustrative purposes only. The cracks formed between each load stoppage are marked in Figure 16 with different colors. The largest number on the legend represents the maximum total applied thrust jack load. Note that crack sizes were not discretely measured on segment D-HC-2 and were only marked at the end of the test following the 10.0 MN load level – progressive crack widths are therefore not included for that segment.

Each segment surface is divided into five regions to quantify the damage states. Regions A, B, D and E are correlated to transverse bursting crack formation, and region C correlates to spalling crack formation. Due to symmetry of loading on the double pad load tests, the crack size development of regions B/D and A/E are plotted together. The results from each segment are identified using the following descriptors: Double/Single pad load – Hybrid/SFRC Concentric/Eccentric – Intrados/Extrados – Cracking region. For example, D-HC-I-A represents the results from the **D**ouble pad load test on the **H**ybrid segment with **C**oncentric loading on the **I**ntrados face in region **A**.

As shown in Figure 16, transverse spalling and bursting cracks were observed on all segments that were taken up to 11.1 MN per pad. Transverse spalling cracks emerged in Region C between the load pads, initiating from the top or bottom of the segment and propagation towards the mid height. Transverse bursting cracks developed under the thrust jack pads (primarily on the extrados face)

and generally initiated under the load pad in the middle of the segment body and propagated towards the top and/or bottom.

A transverse spalling crack on the extrados face of segment D-HC formed first between a load of 4.4 and 6.7 MN per pad. This was followed by the initiation of transverse bursting cracks between 6.7 and 8.9 MN per pad at the mid-height, and these cracks propagated at 10.0 MN and eventually spanned from the top to bottom at a load of 11.1 MN. At the 5.78-MN maximum expected TBM load, no cracks were observed in the D-HC segment. At the 9.55-MN maximum capacity of the TBM jacks, both transverse spalling and bursting cracks were observed but at a width below the allowable limit of 0.2 mm. The transverse bursting crack size exceeded the allowable limit of 0.2 mm between 10.0 and 11.1 MN per pad.

The S-SC segment generally exhibited less crack formation than the D-HC segment. A transverse spalling crack has formed between the segments at a load between 8.9 and 9.6 MN per pad. The transverse bursting crack has formed afterward at a load between 9.6 and 11.1 MN per pad. The crack size in the SFRC segment remain below the 0.2 mm limit up to the maximum applied load of 11.1 MN per pad.

The crack maps and maximum measured crack width development plots indicate that supplemental conventional reinforcement may negatively impact the size of cracks in segments.

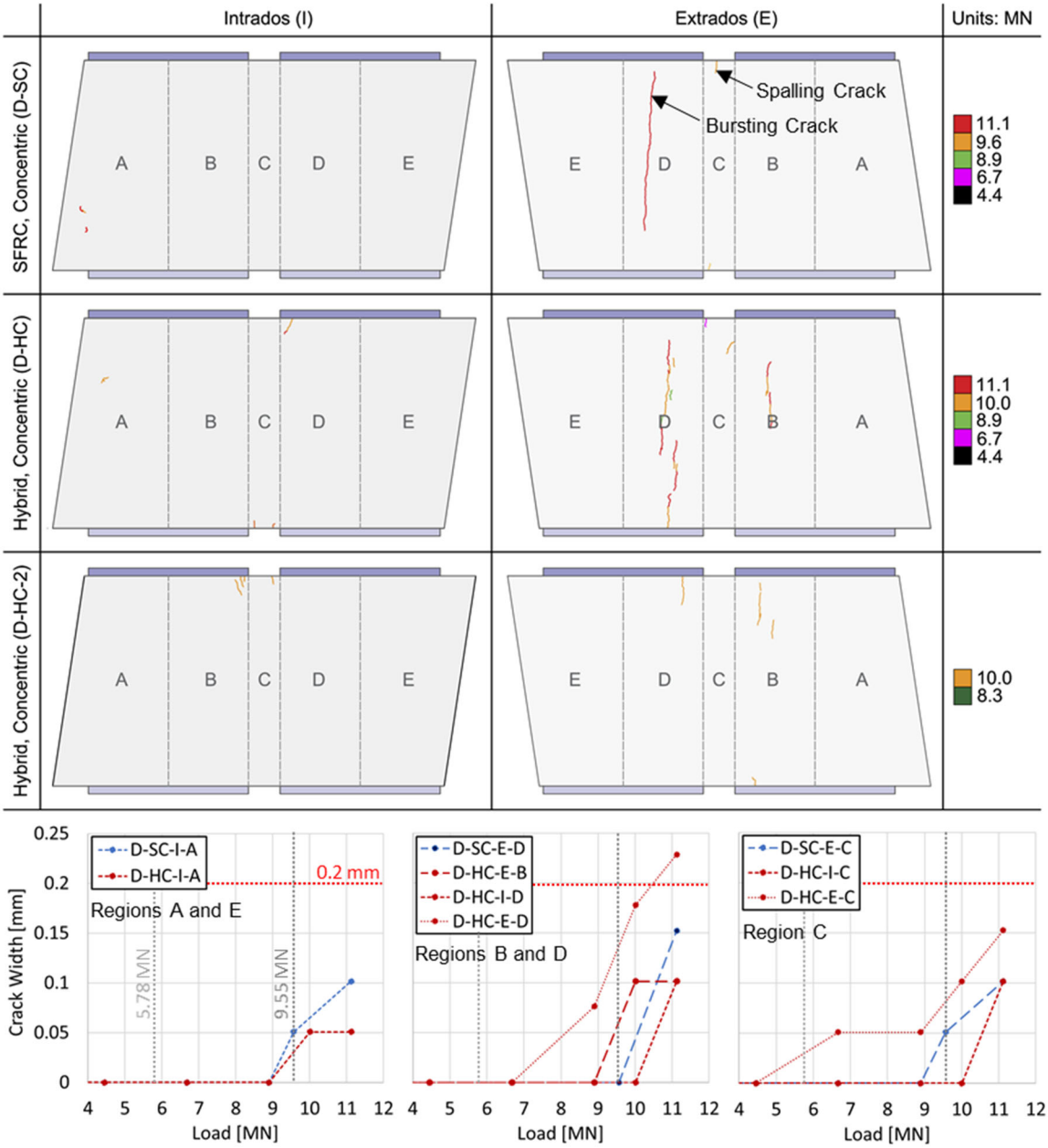

Figure 16: Crack propagation of double pad load tests: mapping on the intrados/extrados faces and plotted as a function of pad load

The achievement of the tensile limits in the spalling and radial and transverse bursting regions has been also examined using strain measurements. Figure 17 summarizes the tensile strain distribution as a function of load and location in these three regions for segments D-HC and D-SC. The figures are also shaded to illustrate the lower and upper bound tension strain limits. The strain development generally matches with the crack propagation shown in Figure 16.

In the SFRC segment, the transverse spalling strains are highest near the top surface and decrease toward the mid height, transverse bursting strains are largest at the mid height, and the radial bursting strains are largest near the load at the top surface. The strain measurements indicate that transverse spalling strains reach the tension strain lower bound first at 4.4 MN per pad followed

by the radial bursting strain and transverse bursting strain between 4.4 and 5.6 MN and 10.0 MN per pad, respectively. These load levels correspond with the numerical predictions for the elastic and inelastic models summarized in Table 5. Furthermore, the location of high strains corresponds to the high strain regions illustrated in Figure 8. These results indicate that the elastic and inelastic FE models provide an approximate, though unconservative, estimate of damage formation in the segment.

The addition of supplemental reinforcement in the Hybrid segment illustrates that the bars have a notable impact on strain development. As expected (as shown in Figure 17) the supplemental conventional steel reinforcement reduces the transverse spalling strain near the top surface. The radial bursting strains are also reduced in the elevated strain region near the top surface. At that location the reinforcement has significant strain levels but the concrete strain is decreased. The transverse bursting strain development under the load pads is not significantly impacted due to the fact that the reinforcing bars are at the edges of the segment and the highest strain region is in the middle of the body. As noted the transverse bursting strain development in both the SFRC and Hybrid segment are similar.

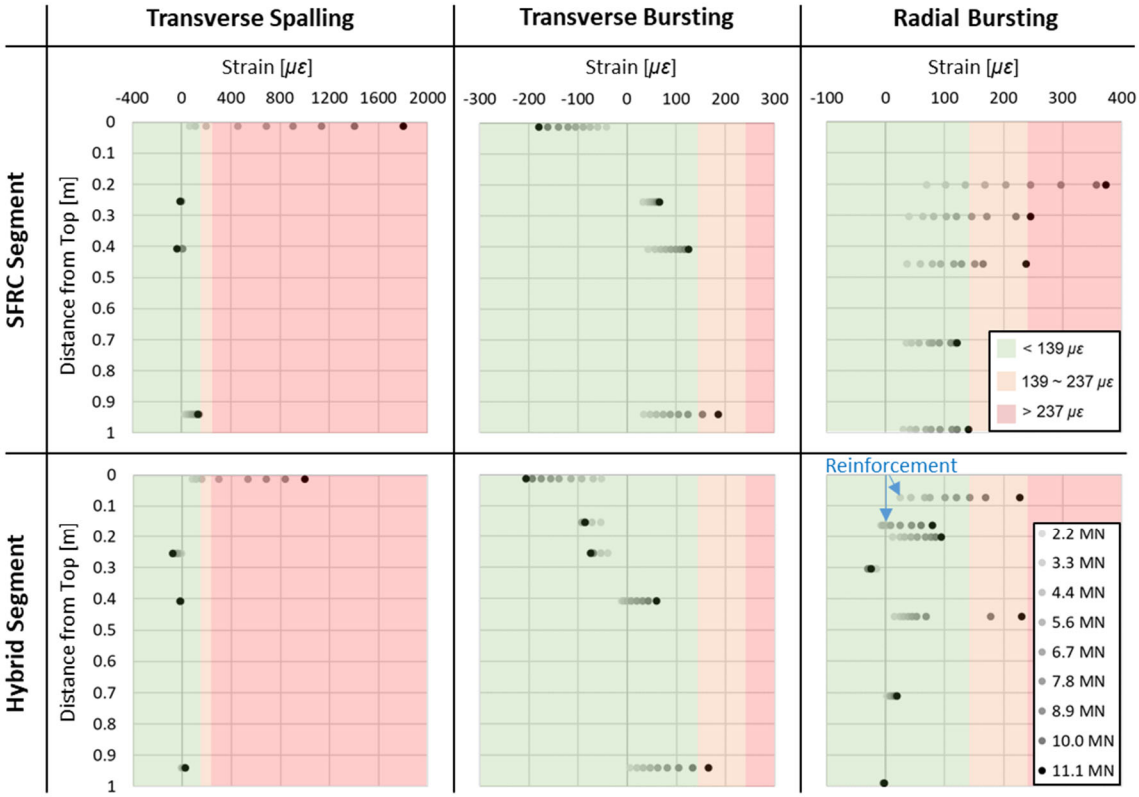

Figure 17: Distribution of strain development on double pad load segments D-HC and D-SC

To provide more insight into the development of damage, the radial strain distributions were measured continuously through the thickness using fiber optic strain gages in the concentric double pad load segment D-SC under both the west and east load pads. The resulting strain distributions as a function of load, distance from the extrados surface, and distance from the top surface are plotted in Figure 18. The strains under the east load pad tend to be marginally higher than the right. The radial strain is highest near the top surface and decreases as you move toward the middle

of the segment (depth 0.20 toward 1.00 m). The strain at the top most measurement (0.20 m from the top) is the highest and exhibits a peak strain near the extrados surface at elevated loads indicating radial crack formation. The strain distributions at the top level compare well with the strain distributions computed using FE methods Figure 8. At the 0.20 m location, the strain is maximum in the segment width and decreases toward the extrados and intrados. At this location, the largest radial strain is approximately ten times the tensile strain limit, indicating potential unobservable internal damage has occurred and the segment could be failing internally due to radial bursting. Based on the strain history the radial strains reached the tensile limit at 197 mm from the intrados at 0.2 m from the top surface. The lower limit of 139 με is reached at a load level of 3.7 MN per pad on the East side and at 6.2 MN on the West side of the segment; the upper limit of 237 με is reached at 6.2 MN per pad on the East side and 8.6 MN on the West side. This is marginally lower than the FE results which reached the lower and upper bound tensile limits at 6.8 and 11.3 MN, respectively. As shown by Iyengar the achievement of cracking at the lower load level may be attributed to non-uniform pressure distribution in the experiment (*41*).

When subjected to relatively low thrust force (e.g. 6.7 MN per pad and lower), the strain along thickness direction distributes relatively uniformly; however, when under high load (e.g. 8.9 MN per pad and higher), the nonuniformity of radial strain distribution appears at the location of 0.2 m from the top surface. At 8.9 MN per pad, nonuniformity of radial strain distribution starts to appear and the maximum strain exceeds the maximum tensile strain limit of 237 $\mu\varepsilon$. At 11.1 MN per pad, the nonuniformity of radial strain distribution becomes more significant, and the largest radial strain is approximately 10 times over the strain limit, indicating potential unobservable internal damage has occurred and the segment could be failed structurally by radial bursting stress if higher thrust jack load applied, while the maximum transverse spalling strain at 11.1 MN per pad is still below the upper tensile strain limit of 237 $\mu\varepsilon$.

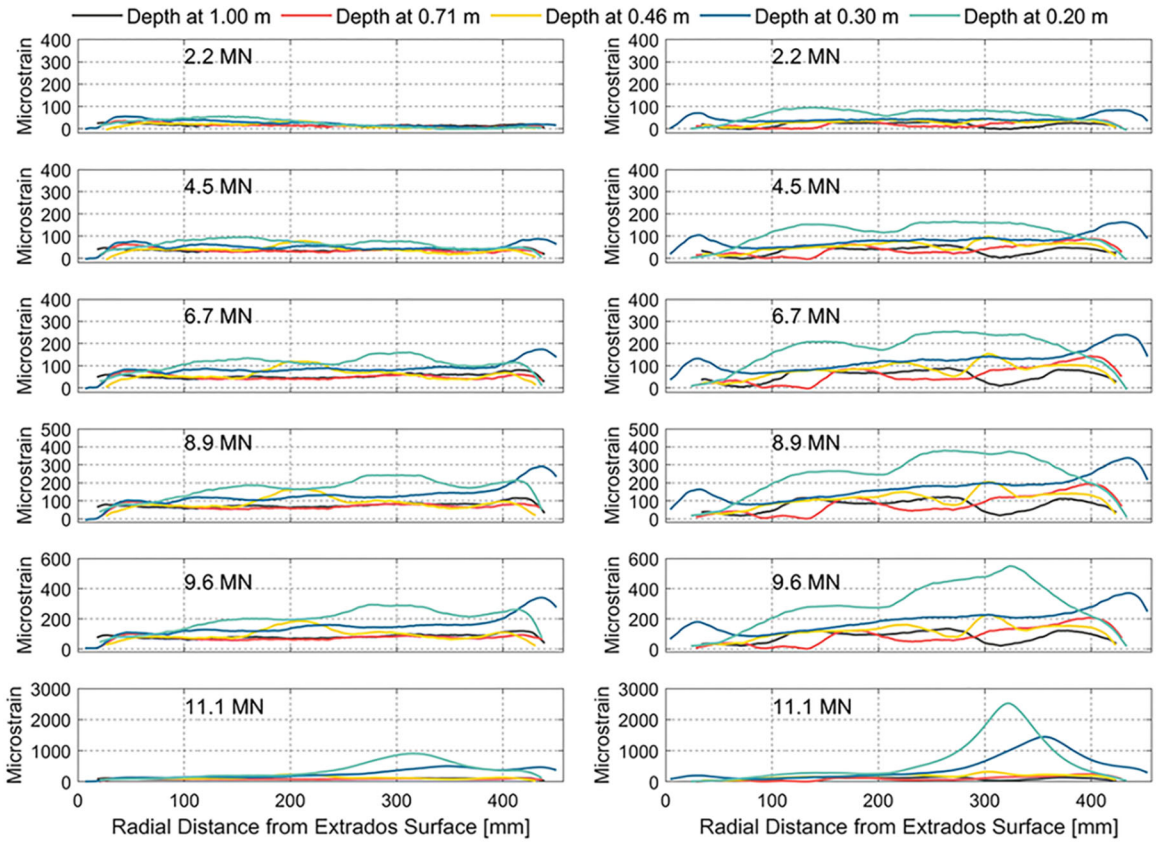

Figure 18: Radial strain distribution in double pad load SFRC segment at west (left) and east (right) sides (Test D-SC)

2.4.2. Ultimate Capacity Assessment (Single Pad Load Cases)

From the double pad load service load assessment, it was found that spalling stress leads to the formation of initial cracks which do not propagate significantly, however, bursting stresses can lead to major damage. To assess the potential governing failure mode, single pad load tests were conducted to provide an overload condition and potentially fail the segment. The effects of supplementary conventional reinforcement and eccentricity were also investigated. Three single pad load tests were conducted: a concentric pad load test on the SFRC segment (S-SC), a concentric pad load test on the hybrid reinforced segment (S-HC), and an eccentric pad load test on the Hybrid segment (S-HE). An eccentricity of 38 mm was used. This value is greater than the 30 mm recommended by AASHTO and less than the 51 mm recommended by the TBM system. This eccentricity was chosen due to limitations on allowable eccentricity in the testing machine at a load of 22.2 MN.

Among the three single pad load tests, only the SFRC segment (Test S-SC) exhibited a failure mode. The segment failed under an applied load of 20.3 MN, which is more than twice the maximum TBM jacking capacity of 9.55 MN per pad and almost four times the maximum expected thrust jack load per pad of 5.78 MN. The failure was abrupt and consisted of separation of the outer edge of the segment as shown in Figure 19. No structural failure was observed in the hybrid-

reinforced segments; however, significant cracks were observed at the highest thrust pad load of 22.2 MN.

(a) (b) (c)

Figure 19: Failure and damage of single pad load test on SFRC segment (Test S-SC): (a) failure induced by radial bursting stress, (b) concrete spall damage due to radial bursting, and (c) cracking caused by transverse bursting stress

The crack propagation of the three single pad load segments, including crack maps and crack width development plots are shown in Figure 20. Each surface is divided into 3 regions, including 2 regions (A and B) under the load pad, where bursting cracks form, and 1 region (C) outside of the load pad, where spalling cracks form. A noticeable difference in cracking damage becomes apparent at 13.3 MN. At this load level transverse bursting crack formation in the SFRC segment becomes more pronounced than that observed in either Hybrid segment. The SFRC segment revealed a distinct ultimate radial bursting stress failure at a pad load magnitude of 20.3 MN. Both hybrid segments did not exhibit an abrupt ultimate radial bursting stress failure. This demonstrates that, while the supplemental reinforcement may negatively impact the formation of cracks it does provide additional resistance against overload radial bursting stresses. The eccentricity of 38 mm towards the extrados surface has no significant effect on cracking performance.

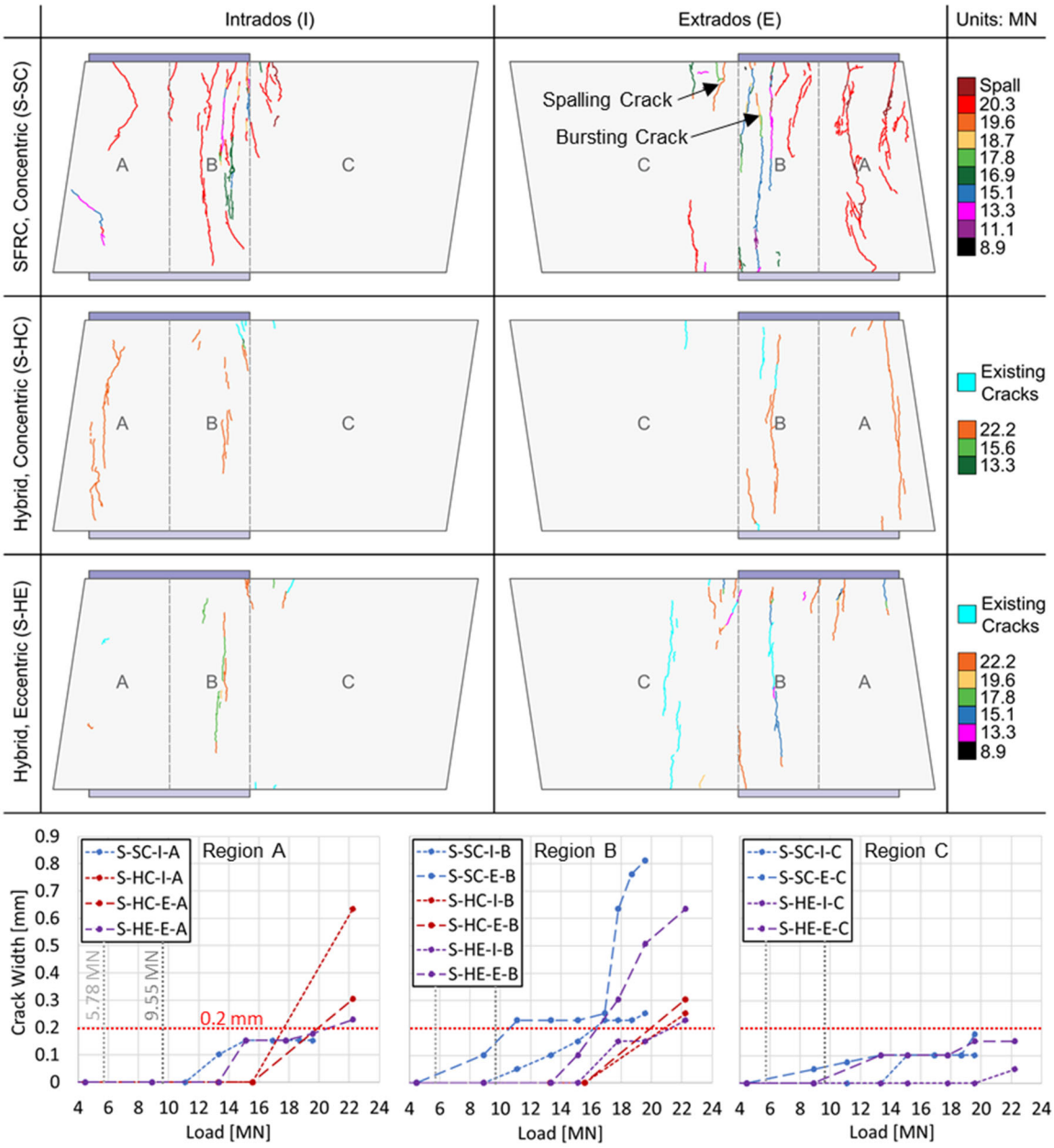

Figure 20: Crack propagation of single pad load tests

Figure 21 summarizes the bursting tensile strain distribution of all single pad load tests. The largest transverse bursting strain generally develops under the load pad at segment mid height similar to the double pad load tests. Unfortunately, the radial strain measurements were not successful for the S-SC segment and are not presented. Comparison of the transverse strain distributions, supplementary conventional reinforcement does not have a significant effect until higher load levels, and associated cracks are formed. The SFRC and hybrid segments exhibit similar distributions up to 15.6 MN. When the thrust jack load is above 13.3 MN, the hybrid segments present a more linear strain development, while the SFRC segment exhibits a significant strain increase. In comparison with the test of concentric single pad load on the hybrid segment, the eccentric load causes significant difference in strain development on the intrados and extrados

faces near the load pads, but the strain difference becomes less when further away from the load pads. This explains the minimal difference observed in the cracking performance between the concentric and eccentric load cases.

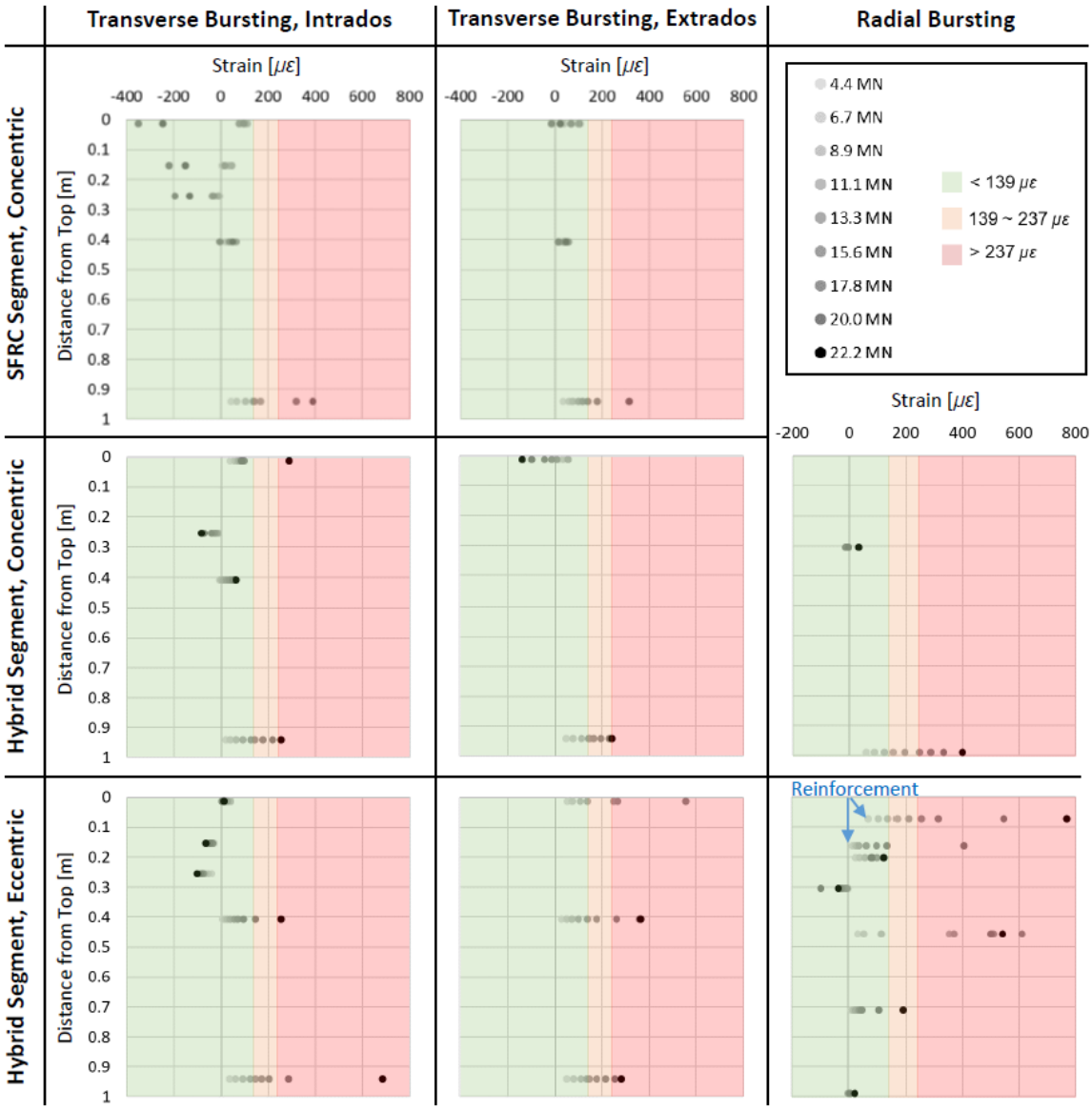

Figure 21: Distribution of (a) intrados transverse bursting strain, (b) extrados transverse bursting strain and (c) radial bursting strain of SFRC and hybrid segments under concentric and eccentric loads

2.5. Conclusions

An experimental study has been conducted to examine the performance of full-scale PCTL segments from a 12.8 m diameter tunnel project subjected to thrust jack loading. Two tests were performed on the segments fabricated with SFRC and four tests were performed on the segments fabricated with SFRC and supplemental steel reinforcement. Segments were loaded with a double pad load configuration beyond the expected thrust demands to assess the performance under the maximum expected thrust jack load and the maximum jacking capacity of the TBM. Single pad

load tests were conducted to examine the performance of the segments at ultimate limit state. Based on the crack and strain development observed the following conclusions can be made:

- Observed crack propagation and strain measurements on the segments match well with expected damage formation from FE analyses. Transverse spalling cracks form first followed by high radial strains (indicative of radial cracking), and lastly by transverse bursting cracks.
- Damage propagation observed is predicted well with both elastic and nonlinear FE models. Due to the relative independence of the transverse spalling and bursting stresses, the elastic model provides adequate accuracy in the prediction of first crack formation and subsequent tensile load limits.
- The SFRC and the hybrid-reinforced segments did not crack when subjected to the maximum expected thrust jack pad load level (5.78 MN per pad). Cracking did occur prior to the ultimate thrust jack pad load (9.55 MN per pad) of the TBM, however, the crack size was less than the AASHTO limit of 0.2 mm.
- The addition of supplementary periphery reinforcement in the hybrid segment results in earlier crack formation. The reinforcement however does provide additional strength against bursting failure due to overload conditions.
- Radial thrust jack load eccentricity of 38 mm towards the extrados surface has no significant influence on the cracking performance caused by bursting stress, according to results of single pad load tests. From the FE models, the effect of eccentricity on spalling stress is expected to be more significant, as the tensile limits are met at significantly lower load for transverse spalling compared to transverse bursting and radial bursting.
- The nonlinear behavior of SFRC under thrust demand generally appears in the transition zone between lower and upper tensile strain limits. As aforementioned, SFRC responds

differently to different types of loading, so a range of tensile limits can better represent the capacity of tunnel lining segments. An inverse analysis based on RILEM provides a good estimate of the lower tensile limit. For general design of SFRC segments, the linear FE models can generally fulfill the needs when using strain limits as criteria.

It should be noted that the test results have some limitations. This includes but is not limited to the fact that measurements were discretely taken and peak strains may exist at lower load levels in other regions of the segment. A stiff loading beam was used to apply the load to the segments, however inherent flexibility may have introduced non-uniform pressure on the double and single pad tests. Additional studies should be conducted to develop an approach to accurately determine cracking in segments due to thrust jack loading.

3. Performance of Skewed Radial Joints in Precast Concrete Segmental Tunnel Linings

3.1. Introduction and Background

Shield tunneling approaches and segmental tunnel lining systems have been increasingly implemented for both highway and transit tunnels, due to their reliable quality, mechanical efficiency, and construction speed (*42*). When under service load, tunnel lining rings are subjected to combinations of axial and flexural demands in the circumferential direction of the liner. Unlike a monolithically cast ring, segmental linings have an overall reduction in stiffness due to the joints between segments (*43*), which impacts the flexural performance of the lining system (*42*). Accurate evaluation of the liner requires proper modeling of the nonlinear response of the joint. Joint rotational stiffness is dependent on the level of axial load, the contact area geometry, and the skew of the joint.

Full-ring experiments have been performed to investigate the overall mechanical behavior of tunnel linings, e.g. stiffness, stability, deformation tolerance and bearing capacity, and also to optimize the design and development of computational models (*44*) (*45*) (*46*) (*47*).

Depending on the depth of the tunnel and in-situ stresses, the axial and flexural demands along circumferential direction vary significantly. The differences in the axial force and bending moment can result in diverse nonlinear joint response (*43*). Studies with various combinations of the axial force and bending moment have been conducted on perpendicular radial joint assemblies with two segments to evaluate the joint response under specific loading conditions. Moment-rotation responses are generally examined to evaluate the flexural performance of tunnel radial joints under various combinations of axial load (N) and bending moment (M) as shown in Figure 22. Experimental studies have been conducted under constant axial load with varying moment (*48*) (*49*) (*50*) (*51*), under constant *M*/*N* ratios (*52*), and under loading conditions comparable to in-situ construction and operation loads (*53*).

Zhang and Zhao (*54*) evaluated the flexural performance of tunnel key segments with a 2° skewness, where the test assembly consisted of three segments, including one key segment, and two cut adjacent segments. However, no available study that investigates the rotational behavior of skewed radial joint assemblies with conventional two segment configuration has been found. Tunnel segments in this study are designed with an 8° radial joint skew to facilitate the appropriate longitudinal alignment. Though an increasing number of shield tunnel projects have implemented segments with skewed radial joint (*55*), no study has evaluated the rotational behaviors of individual skewed radial joints under various axial load level, where the experimental rotational behaviors of radial joints are critical for optimization of numerical modeling and design of tunnel radial joints.

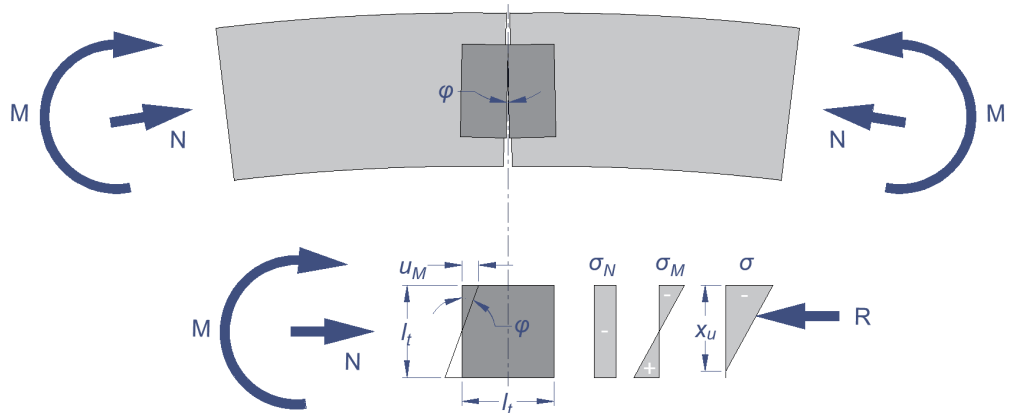

Figure 22: Illustration of positive moment-rotation and Janssen's model (*1*)

Other than the influence from joint skewness, the effects of bolting are suggested to be researched for radial joints by U.S. Federal Highway Administration, and it is also recommended the analysis should be correlated with applied axial force and bending moment (*55*). In practice, the bolts are installed to connect and align segments during construction phase, and sometimes will be removed when tunnels are constructed to prevent falling out from sockets after long-term dynamic loading from the vibration induced by traffic, and even earthquake loading. Li et al (*51*) evaluated the effect of bolt prestress (tightening force) on the rotational behavior of tunnel radial joints; however, there is no available study that has examined the rotational behavior of radial joints without bolts, where in design the stiffness from bolts is generally neglected.

For design purposes, computational models generally consider the radial joint as a rotational spring, with reference to joint dimensions, closed/opened joint and material plasticity (*1*) (*7*) (*56*) (*51*) (*57*). Janssen (*1*) initiated a theoretical solution based on flexural bearing and decompression of an elastic concrete joint, allowing for the determination of the joint moment-rotation behavior as a function of the applied axial force and can be used for modeling the response of a tunnel subject to external loads transverse to the longitudinal axis of the tunnel. Other models have optimized Janssen's theoretical solutions with the consideration of more realistic material properties, i.e. concrete plasticity and effects of confined concrete (*7*) (*56*) (*51*) (*57*). The Janssen model assumes that the contact area can be modeled as a concrete beam with the same dimensions as contact area, with zero tensile stress capacity (*7*). The configuration and assumptions of Janssen's model are illustrated in Figure 22. When under the combination of the axial load, *N*, and bending moment, *M*, the joint rotates at an angle of φ ($= u_M/l_t$), and whether the joint is closed or opened depends on whether the magnitude of flexural stress, σ_M, caused by *M* exceeds the magnitude of compressive stress, σ_N, caused by *N*. Note that Janssen's theoretical solutions have not considered the stiffness from the bolts and gasket that generally used in practice.

This study examines the rotational behaviors, e.g. moment-rotation and rotational stiffness, of 8-degree-skewed joints at various axial load levels, from 674 to 2250 kN/m. Two individual assemblies were tested to determine the effects of bolting, by estimating the elastic rotational stiffness on the assemblies with and without bolts, at the axial load levels of 674, 1070, 1460, 1850 and 2250 kN/m. After elastic testing, the assemblies were tested under positive bending moment at the axial load levels of 674, 1460 and 2250 kN/m, to determine the rotational behaviors at large rotation level. Two negative bending tests were performed after previous inelastic positive bending tests, to assess the stiffness loss due to potential joint damage. Janssen's theoretical solutions are

presented, and compares with the observed experimental results. Details on the mechanics of the Janssen model are provided in following section, and the theoretical solutions are compared with experimental results.

3.2. Properties of Segments and Radial Joints

The material properties and mix design of SFRC are discussed in Chapter 2.2.1. The segments acquired for this experimental program were fabricated for a tunnel currently under construction in the U.S. The tunnel is approximately 1.6 km in length, with an external diameter of 12.80 m and an internal diameter of 11.89 m. The thickness of the tunnel lining is 457 mm. Each tunnel lining ring consists of 10 concrete segments in each ring assembly, including eight curved parallelogram segments, one large curved trapezoid segment, and one small curved trapezoid key segment, and approximately 900 rings along tunnel direction. The segments are connected with radial bolts after alignment during construction phase, and removed after completion of construction. As shown in Figure 23, the radial joints of the tunnel lining are designed with an 8° skewness to facilitate the appropriate alignment. The segment lengths in the tunnel direction range from 1.93 m to 2.03 m, and in the circumferential direction approximately 4.09 m for the large segments and 1.96 m for the key segments. From earth pressure, the segmented ring will deform from an as-designed circular shape to an oval shape. The allowable ovality of the entire ring is 0.4%, leading to a 0.408° (0.00684 rad) factored maximum rotation at a single joint in the extreme case.

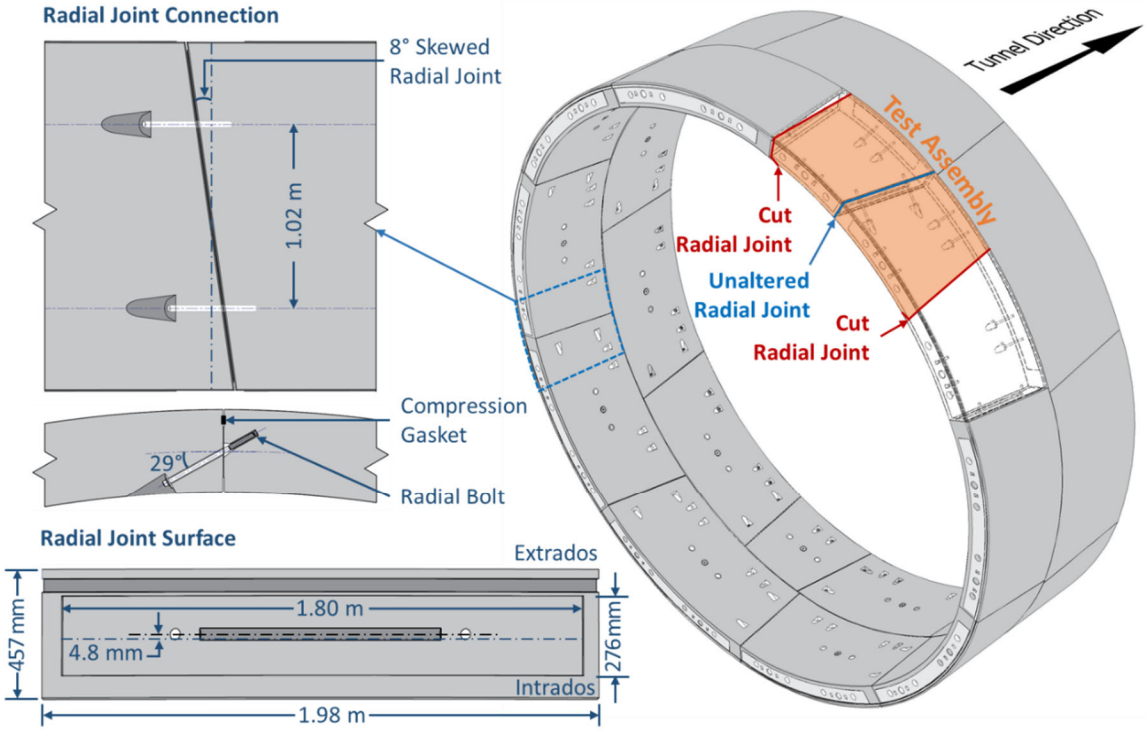

Figure 23: Joint connection of the tunnel where segments were obtained

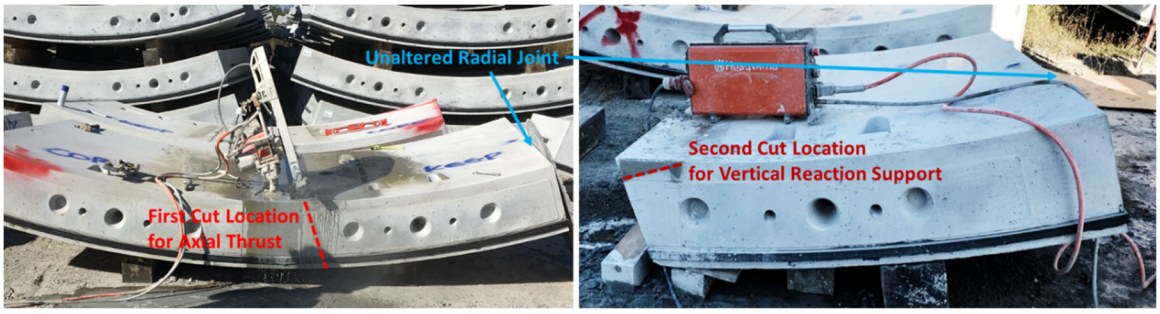

Figure 24: On-site segment cutting based on test assembly

The test assembly consists of a joint between two modified full-scale segments, as presented in Figure 23. To facilitate application of axial load and vertical reaction supports, the segments were cut as illustrated in Figure 24. The first cut on segments were intended to allow for axial thrust application in the circumferential direction, and the second cut was made to create a flat surface for vertical reaction support in the setup. As shown in Figure 23 and Figure 24, the full-size segments were cut to a length of 1.8 m long circumferentially, and radial joint contact area remained unaltered. The unaltered joint surfaces of the tested segments are shown in Figure 25, which consist of 4-mm raised concrete sections as the joint contact area, compression gaskets, radial guide rods, receiving grooves, radial bolt pockets and sockets.

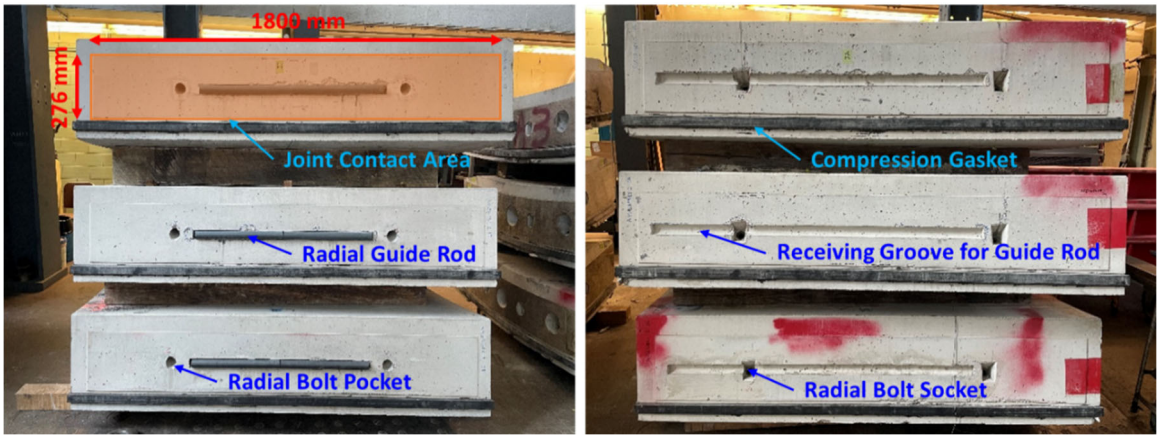

Figure 25: Radial joint details from test sections

3.3. Theoretical Moment-Rotation Model

Theoretical moment-rotation models, based on Janssen's closed-form solutions, are presented to compare with the test results and verify the applicability of Janssen's solutions for predicting rotational behavior of skewed joint. Janssen's solutions was then modified to include radial bolts and compression gasket. The results show that radial bolts and compression gasket has no significant influence on the joint rotational behavior.

3.3.1. Janssen's Theoretical Moment-Rotation Model

As shown in Figure 22, Janssen's theoretical solutions for estimating joint rotational behaviors are based on flexural bearing and decompression of an elastic concrete section, with the dimensions of the joint contact area and no tensile capacity (*7*). The joint moment-rotation behavior can be

written as a function of the axial force applied and can be used for modeling the response of a tunnel subject to external loads transverse to the longitudinal axis of the tunnel. The derivation of Janssen's model, documented in German in Janssen (*1*), is summarized in English by Groeneweg (*7*). Janssen's moment-rotation model can be expressed as:

$$M_{closed} = \frac{b \cdot l_t \cdot E_c}{12} \cdot \varphi \ (closed\ joint) \qquad \text{Equation 4}$$

$$M_{opened} = \left(1 - \sqrt{\frac{8 \cdot N}{9 \cdot b \cdot l_t \cdot E_c \cdot \varphi}}\right) \cdot \frac{N \cdot l_t}{2} \ (opened\ joint) \qquad \text{Equation 5}$$

where M is the applied moment at the joint; N is the applied axial force (i.e., normal force), ranged from 674 to 2250 kN/m; φ is the joint rotation (in rad); E_c is the elastic modulus of concrete, which is 30940 MPa; b is the length of the joint, which is 1800 mm; and l_t is the height of the joint, which is 276 mm.

The initial linear rotational stiffness before joint opening can be expressed as:

$$k_{joint,closed} = \frac{b \cdot l_t \cdot E_c}{12} \ (closed\ joint) \qquad \text{Equation 6}$$

$$k_{joint,opened} = \frac{9 \cdot b \cdot l_t \cdot E_c \cdot M}{8 \cdot N} \cdot \left(\frac{2 \cdot M}{N \cdot l_t} - 1\right)^2 \ (opened\ joint) \qquad \text{Equation 7}$$

The theoretical linear-elastic rotational stiffness of the segment before reaching cracking moment is assessed to compare with the linear rotational stiffness, which can be expressed as:

$$k_{segment} = \frac{w \cdot t \cdot E_c}{12} \qquad \text{Equation 8}$$

where w is the width of the segment, which is 1980 mm; t is the thickness of the segment, which is 457 mm.

As aforementioned, opening of the compressed joint initiates when the strain at the extreme fiber reaches zero (i.e. $\sigma_M > \sigma_N$). This can be determined using either the closed or open joint moment-rotation relationships. The rotation at incipient joint opening or the ratio of moment to axial force that would result in incipient joint opening is given by Equation 9:

$$\varphi \geq \frac{2 \cdot N}{b \cdot l_t \cdot E_c} \left(or\ \frac{M}{N} > \frac{l_t}{6}\right) \qquad \text{Equation 9}$$

Equation 9 indicates that the joint stiffness transitions from linear behavior to nonlinear behavior once the axial (i.e. normal) force is no longer within the core of the contact area. This occurs when the ratio of applied moment to axial force (i.e., the eccentricity) is larger than 1/6 of joint height. Janssen's theoretical solutions are used as a comparison in the following presentation of experimental results. Note that a number of assumptions inherent in the model do not accurately represent the actual joint tested, as it does not consider the presence of the skewed joints, the radial bolts and the compression gaskets, and the general assumption that the joint is fully closed under all axial load levels, and the reduced bearing area due to the receiving grooves for the radial guide rod.

3.3.2. Modified Janssen's Model with Gasket and Bolts

As shown in Figure 26, Janssen's model was modified with gasket and bolts as spring elements. With normal force and bending moment applied, the rotation causes forces developed in the bolts and gasket, F_G and F_B. The initial force in the gasket and bolts, $F_{G,0}$ and $F_{B,0}$, are assumed to be zero. The gasket has a stiffness, K_G, of 11705 kN/m/m. The bolt has a diameter of 25 mm and a free length of 392 mm from the inside of the bolt head to the socket when installed. The measured yield strength based on a single test of a bolt is 630 MPa, and the measured elastic modulus is 245 GPa. The resulting stiffness of 2 bolts, K_B, are 632 MN/m.

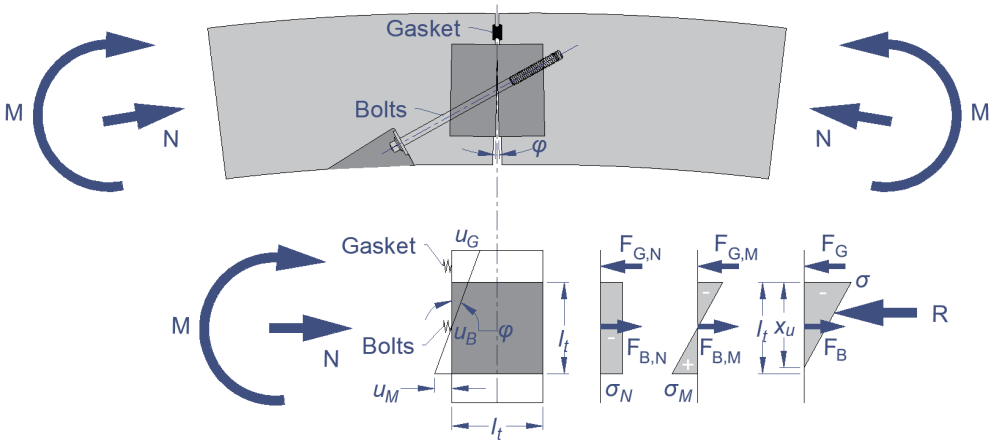

Figure 26: Illustration of positive moment-rotation and Janssen's model

The force in the gasket and bolts due to positive bending can be expressed as:

$$F_G = F_{G,0} + K_G \cdot u_G \text{ (Compression in Positive)} \qquad \text{Equation 10}$$

$$F_B = F_{B,0} + K_B \cdot u_G \text{ (Tension in Positive)} \qquad \text{Equation 11}$$

The reaction force in the concrete joint section is:

$$R = N - F_G + F_B \text{ (Compression in Positive)} \qquad \text{Equation 12}$$

The initial linear rotational stiffness before joint opening is the same as basic Janssen's model; however, due to the forces in gasket and bolts, the rotation at incipient joint opening or the ratio of moment to axial force that would result in incipient joint opening is given by Equation 13:

$$\varphi \geq \frac{2 \cdot R}{b \cdot l_t \cdot E_c} \left(or \ \frac{M}{R} > \frac{l_t}{6} \right) \qquad \text{Equation 13}$$

Based on equilibrium, the moment is given by Equation 14, where d_G is the distance from the joint center to the gasket, and d_B is the distance from joint center to the bolts.

$$M = R \cdot \left(\frac{l_t}{2} - \frac{x_u}{3} \right) + F_G \cdot d_G - F_B \cdot d_B \qquad \text{Equation 14}$$

The depth in contact is given by Equation 15:

$$x_u = \frac{2 \cdot R}{\sigma \cdot b} \qquad \text{Equation 15}$$

By substituting Equation 15 into Equation 14, the stress at the joint top is given by Equation 16:

$$\sigma = \frac{4 \cdot R^2}{3 \cdot b \cdot (l_t \cdot R + 2 \cdot (F_G \cdot d_G - F_B \cdot d_B - M))} \quad \text{Equation 16}$$

The displacement at the joint top due to normal force and bending moment is given by Equation 17:

$$u = \varepsilon \cdot l_t = \frac{\sigma}{E_c} \cdot l_t = \frac{4 \cdot l_t \cdot R^2}{3 \cdot E_c \cdot b \cdot (l_t \cdot R + 2 \cdot (F_G \cdot d_G - F_B \cdot d_B - M))} \quad \text{Equation 17}$$

The displacements at gasket and bolts can be expressed as:

$$u_G = \frac{d_G + x_u - {}^{h}/_{2}}{x_u} \cdot u \quad \text{Equation 18}$$

$$u_G = \frac{d_B + x_u - {}^{h}/_{2}}{x_u} \cdot u \quad \text{Equation 19}$$

The rotation after joint opening can be then expressed as:

$$\varphi = \frac{u}{x_u} = \frac{8 \cdot l_t \cdot R^3}{9 \cdot E_c \cdot b \cdot (l_t \cdot R + 4 \cdot (F_G \cdot d_G - F_B \cdot d_B - M))^2} \quad \text{Equation 20}$$

The moment can be expressed as:

$$M = R \cdot \left(\frac{l_t}{2} - \sqrt{\frac{2 \cdot l_t \cdot R}{9 \cdot E_c \cdot \varphi \cdot b}} \right) + F_G \cdot d_G - F_B \cdot d_B \quad \text{Equation 21}$$

Based on the normal force, N, reaction force at concrete joint section, R, and forces in gasket and bolts, F_G and F_B, the moment-rotation behavior can be determined through numerical approximation. The theoretical moment-rotation behavior at the axial load levels 674, 1460 and 2250 kN/m are summarized in Figure 27. Four curves, including basic Janssen's model, Janssen's model with only bolts, Janssen's model with only gasket and Janssen's model with both bolts and gasket, are plotted for each axial load level, to compare the effect of gasket and bolts.

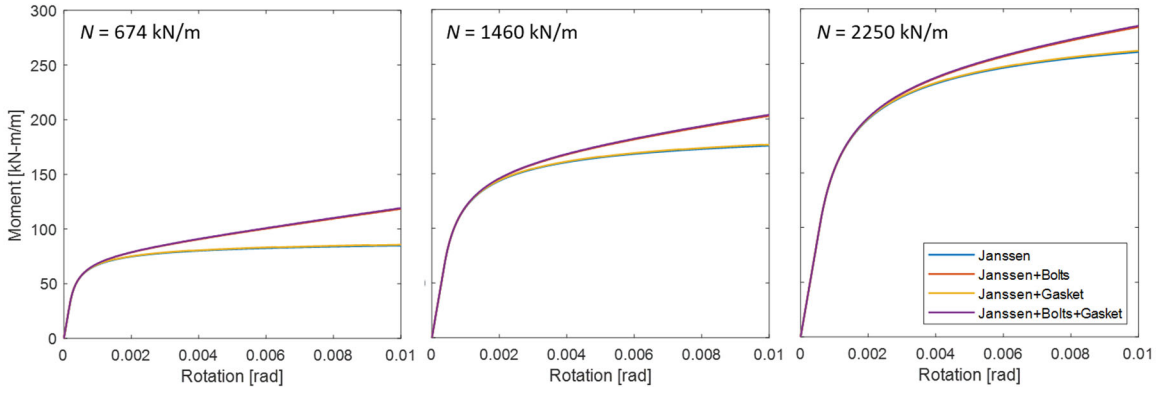

Figure 27: Theoretical moment-rotation behavior at 674, 1460 and 2250 kN/m axial load level

The gasket has no significant influence on the joint rotational behavior. The bolts increase the rotational stiffness at larger rotational levels, and this effect becomes larger at lower axial load levels. Janssen's basic model gives conservative estimation of joint rotational behavior by neglecting the effect of gasket and bolts. As gasket and bolts do not cause drastic difference in joint rotational behavior, the basic Janssen's model without gasket or bolts have been used for comparison with test results.

3.4. Experimental Program

A series of radial joint tests were performed on three joint assemblies of SFRC segments. A joint test assembly consists of two cut panels and one unaltered joint as shown in Figure 28. The joints were tested with and without radial bolts. The tests consist of moment-rotation determination at constant axial load levels. A number of different axial load levels were examined including 674, 1070, 1460, 1850 and 2250 kN/m. Both positive and negative bending tests were performed to determine the initial elastic moment-rotation responses. To ensure that the joint remained elastic under the stiffness evaluation the moment demand for each axial load level was limited to ensure that the stress at the extreme compression fiber remained below 40% of the expected compressive strength. Nonlinear-inelastic joint behavior was examined through positive bending tests, when subjected to axial force levels of 674, 1460 and 2250 kN/m. The behavior of damaged joints was examined through negative bending tests at the axial force levels of 1460 and 2250 kN/m following the previous nonlinear-inelastic positive bending testing. Note that the nonlinear-inelastic joint behavior tests were only conducted in the positive bending direction, and the damaged joint behavior tests were only conducted in the negative bending direction. For clarity, positive bending is defined in this study as producing compression on the extrados and decompression/opening on the intrados of the joint, and negative bending is defined as producing compression on the intrados and decompression/opening on the extrados of the joint. The matrix of assemblies and the description of the tests conducted on each are summarized in Table 7.

Table 7: Test Matrix

Assembly	Description
Assembly 1	1. Calibration and non-destructive evaluation of setup and loading scheme 2. Positive $M-\varphi$ at N= 1460 kN/m axial load with radial bolts 3. Positive $M-\varphi$ at N = 674 kN/m axial load with radial bolts
Assembly 2	1. Negative/Positive joint rotation stiffness evaluation at N = 674, 1070, 1460, 1850 and 2250 kN/m axial load with radial bolts 2. Positive $M-\varphi$ at N = 2250 kN/m axial load with radial bolts 3. Negative $M-\varphi$ at N = 2250 kN/m axial load with radial bolts
Assembly 3	1. Negative/Positive joint rotation stiffness evaluation at N = 674, 1070, 1460, 1850 and 2250 kN/m axial load without radial bolts 2. Positive $M-\varphi$ at N = 1460 kN/m axial load without radial bolts 3. Negative $M-\varphi$ at N = 1460 kN/m axial load without radial bolts

3.4.1. Testing Assembly

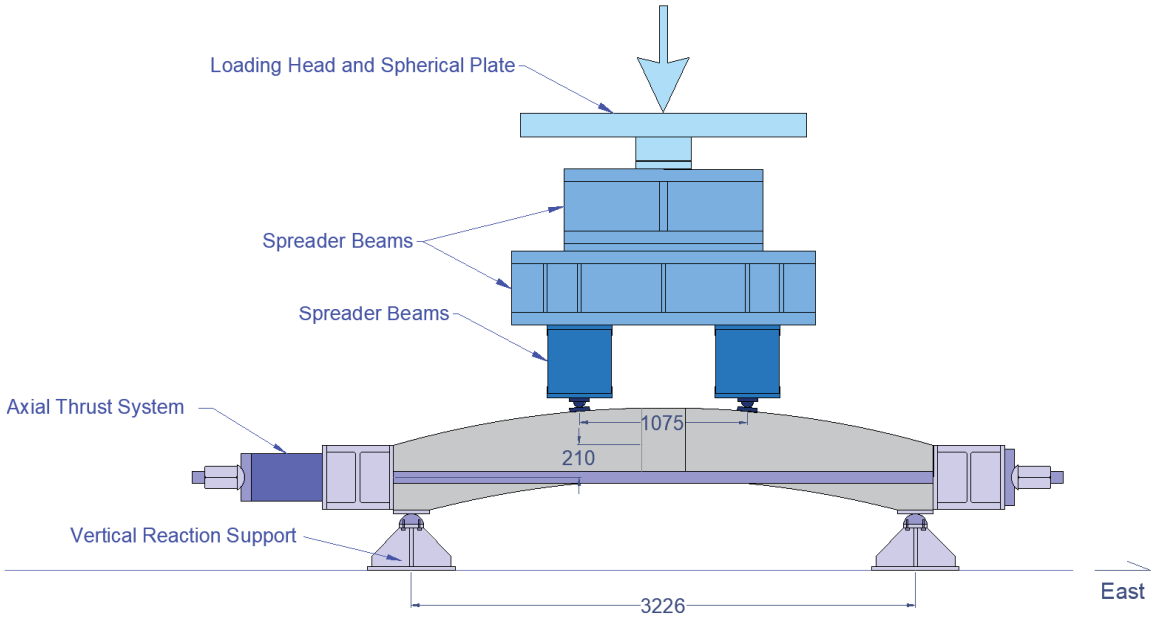

Figure 28: Test configuration (units: mm)

The axial and bending loads at the radial joint were simulated by connecting two segments into an assembly. The radial joint and segment ends comprising the joint was unaltered. The axial thrust was applied with two 1.3 MN capacity through-hole jacks which provided horizontal loading using two outbound post-tensioning bars as shown in Figure 28. The axial load was applied to the cut surfaces, which were fabricated perpendicular to the ring's circumferential axis. Joint flexure was generated simultaneously by the eccentric axial load and a vertical load applied using a Baldwin 22 MN capacity universal testing machine. The vertical load was spread to create third-point flexural loading on the segments. The photos of test configuration are illustrated in Figure 29.

Figure 29: Radial joint test assembly: west side (left) and east side (right)

To apply joint moment with constant axial load on the assembly, a multistep loading procedure was conducted. The joint assembly geometry, applied vertical force, F_y, axial force, F_x and dimensions including eccentricity, e, are shown in Figure 30. The test initialized with alignment of the panels using temporary vertical jacks and installation of the radial bolts loosely in their pockets. The axial thrust system was then engaged to apply adequate axial load to overcome the moment at the joint induced by self-weight of the segment. The axial load was then stepwise increased to the target axial thrust force needed for each test. During each step the negative bending moment generated by the eccentricity of the axial load was counterbalanced by a vertical load, applied through the universal machine, to ensure that a net zero moment was present at the joint. When radial bolts were used in a test, they were tightened when a target axial load of 674 kN/m was achieved. This level was chosen based on preliminary observations which indicated that the gap between the two segments generated by the gasket compression, was closed. Once the target axial load was reached, the axial jacks were set to maintain constant pressure/load, and joint flexure was applied using the vertical force application from the universal test machine. Negative bending moment was facilitated by reducing the vertical load, while positive bending moment was facilitated by increasing the vertical load on the segments. The vertical loads were applied at a rate between 22 and 89 kN/min.

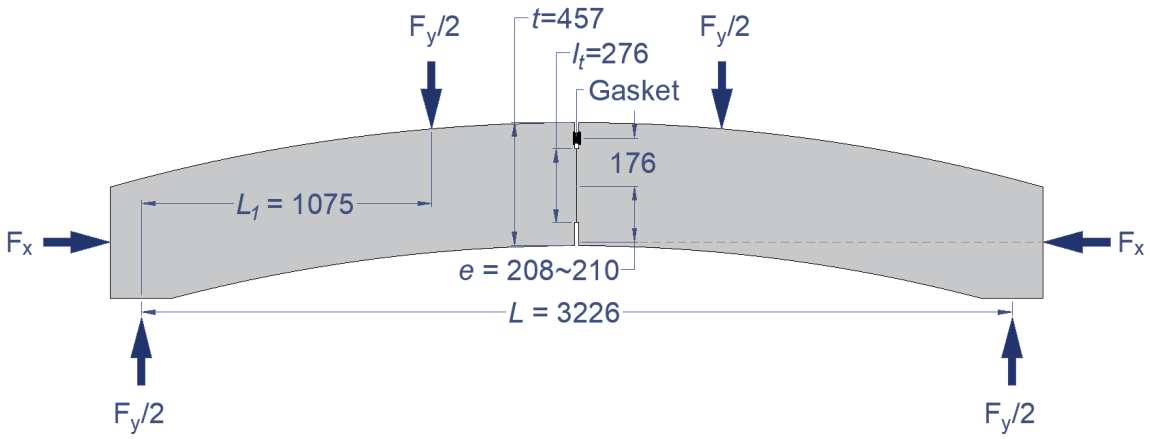

Figure 30: Load application configuration

The test configuration shown in Figure 28 can be simplified to the loading schematic shown in Figure 30. The vertical load, F_y, provides positive bending moment, and the horizontal load, F_x, due to its eccentricity, provides negative bending moment. The eccentricity of the joint ranges from 208 to 210 mm along the skewed joint, and an average value of 209 mm is selected for moment calculations. The self-weight of each segment is estimated to be 37.4 kN.

3.4.2. Instrumentation

Assemblies were outfitted with linear variable differential transformers (LVDTs) to measure joint openings, rotation meters to compare with LVDT data, displacement transducers for monitoring purposes, and strain gages to measure the concrete surface strain and the strain in the radial bolts. The layout of LVDTs (L*), vertical and horizontal displacement transducers (VD* and HD*) and rotation meters (R*) are shown in Figure 31. The bolt strain gauges were installed in a 1-mm predrilled hole at the depth of 64 mm from the bolt head. The surface bonded strain gages were installed at 203 mm from the middle of radial joint, in order to assess whether the joint is closed. The locations of surface bonded strain gages were determined by the load distribution angle of 22.5˚, based on the linear stress distribution in local zone (*4*). At 203 mm from the joint, the compressive stress due to axial force is expected to be distributed linearly.

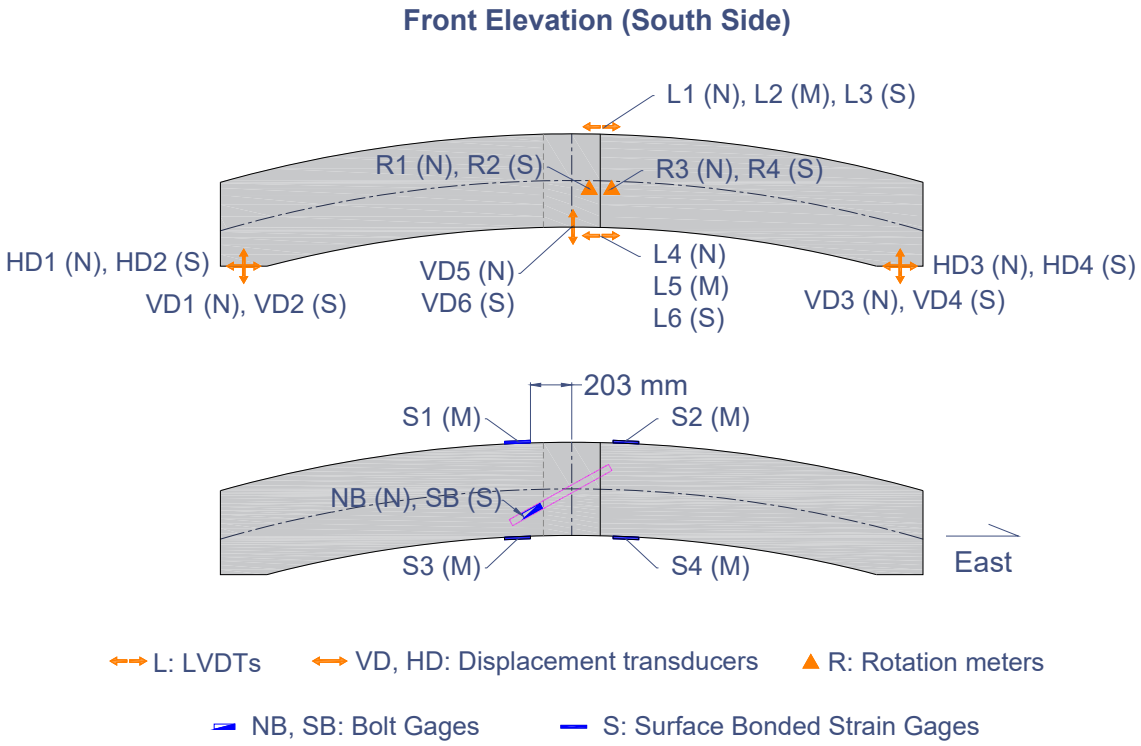

Figure 31: Assembly instrumentation layout (N: North, M: Middle, S: South)

The rotation was measured through LVDTs, while the rotation meters were only used as a reference to compare with the LVDT data due to relatively low precision. The measured average joint was computed from the six LVDTs along the joint as noted in the following expression:

$$\varphi = \frac{1}{3} \cdot \left(\frac{(L_4 - L_1)}{d_1} + \frac{(L_5 - L_2)}{d_2} + \frac{(L_6 - L_3)}{d_3} \right) \qquad \text{Equation 22}$$

where L_1 through L_6 are the displacement measured by LVDTs, and d_1 through d_3 are the measured distances between extrados and intrados LVDTs, which was approximately 533 mm.

3.4.3. Gasket and Radial Joint Bolt Properties

The gasket and joint bolt properties were measured to determine their stiffness and strength. Datwyler glued Wesertunnel gaskets were used. A pair of gasket samples 76 mm long were installed in a 3D printed bracket and tested in compression. The pair of gaskets were loaded eight times with each test stopping after the effective radial joint surface was in contact. The force-displacement relationships are plotted in Figure 32, and averaged. The average force to close the initial 17.5 mm gap produced by the gasket height is 53.2 kN/m.

The radial joint bolts were provided by Optimas. The bolt system consists of an embedded socket and an ASTM A325 bolt. The bolt has a diameter of 25 mm and a free length of 392 mm from the inside of the bolt head to the socket when installed. The minimum specified yield strength is 480 MPa and the specified tensile strength is 724 MPa. Based on a single test of a bolt a yield strength

of 630 MPa and tensile strength of 846 MPa was measured. Both values exceed the minimum required.

$$M = \frac{F_y \cdot L_1}{2} - F_x \cdot e + \frac{W \cdot L}{4} \ (F_x = N) \qquad \text{Equation 23}$$

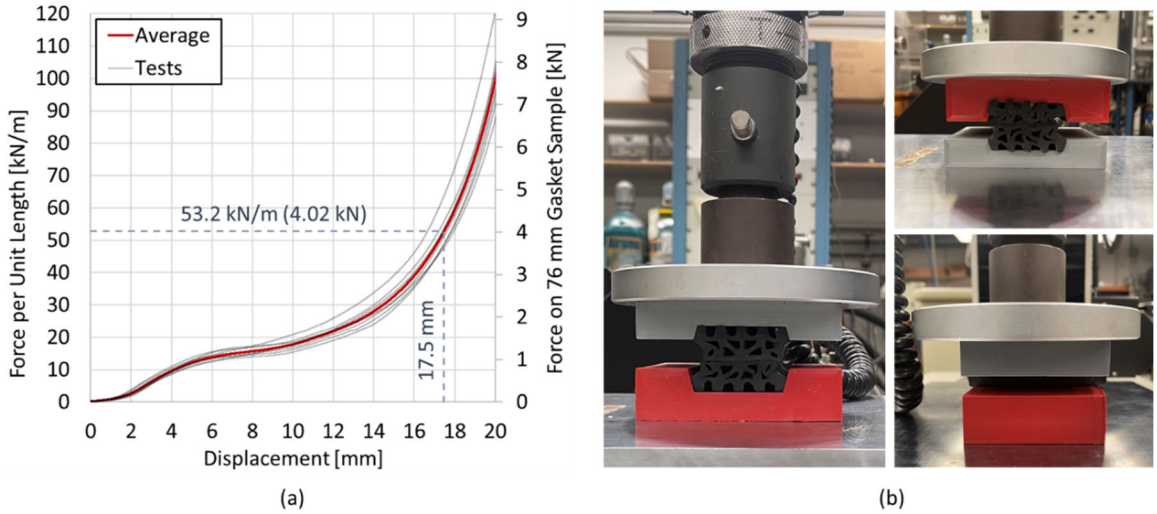

Figure 32: Force-displacement curves of gasket (a) and testing of gasket samples (b)

3.5. Results and Discussion

Three identical assemblies were used to characterize radial joint behavior through a series of tests. The rotational behavior is compared to the commonly used theoretical joint model developed by Janssen (*1*). The rotation criterion from Equation 9 is used to determine the secant rotational stiffness from experimental results. Once the rotation exceeds the rotation criterion, the joint is assumed opened and exhibit nonlinear rotational behavior. During nonlinear opened joint response, the joint rotational behavior is then controlled by the axial force at the joint, and the rotational stiffness generally increases with axial force. The experimental results show the similar trend compared to Janssen's model, but the variation is significant when the axial load level is relatively low. The details of the following are illustrated in the following.

Table 8: Average Strain and Stress Difference

Load Level (kN/m)	Strain Difference ($\mu\varepsilon$)	Stress Difference (Pa)
674	0	0
1070	2	62
1460	26	804
1850	30	928
2250	45	1392

As noted in Figure 31, surface strains were measured on the intrados and extrados surfaces near the joint. The average strain difference between the two surfaces was measured at each axial load level prior to application of joint rotation. The average strain difference, as well as the corresponding average stress difference, at neutral state (i.e., net zero moment) are summarized in Table 8. The average strain difference is the average strain values of the intrados strain gages S3 and S4 subtract the average strain values of the extrados strain gages S1 and S2 (i.e., $\frac{S3+S4}{2} - \frac{S1+S2}{2}$). Note that the strain data has been zeroed at 674 kN/m axial load level. The average stress/strain at the intrados surface is slightly larger than the extrados surfaces. This can be contributed to the distance from joint to intrados surface is less than to the extrados surface, as shown in Figure 23. The average strain difference is then used to determine the average stress difference, by multiplying the elastic modulus. The stress difference between the intrados and extrados surfaces was less than 1.39 kPa for the test series. This indicates that the joints were fully closed prior to the application of joint rotation.

3.5.1. Elastic Rotational Stiffness Evaluation

The results of the elastic rotational stiffness are assessed by examining the moment-rotation results generated at different axial load levels. The moment-rotation ($M - \varphi$) behavior of these joints with and without bolts at five axial force load levels are presented in Figure 33 to Figure 37. The Janssen model predictions are included to provide a relative comparison for each test. The rotation at which each joint is expected to decompress and open is computed based on the axial load level and the estimated elastic concrete modulus as discussed in Chapter 3.3.1 and expressed in Equation 9. The nonlinear responses at large rotation are due to decompression and opening of the joint, and the high stiffness at the beginning can be contributed to the delayed response from axial thrust system when the vertical load suddenly increases/decreased.

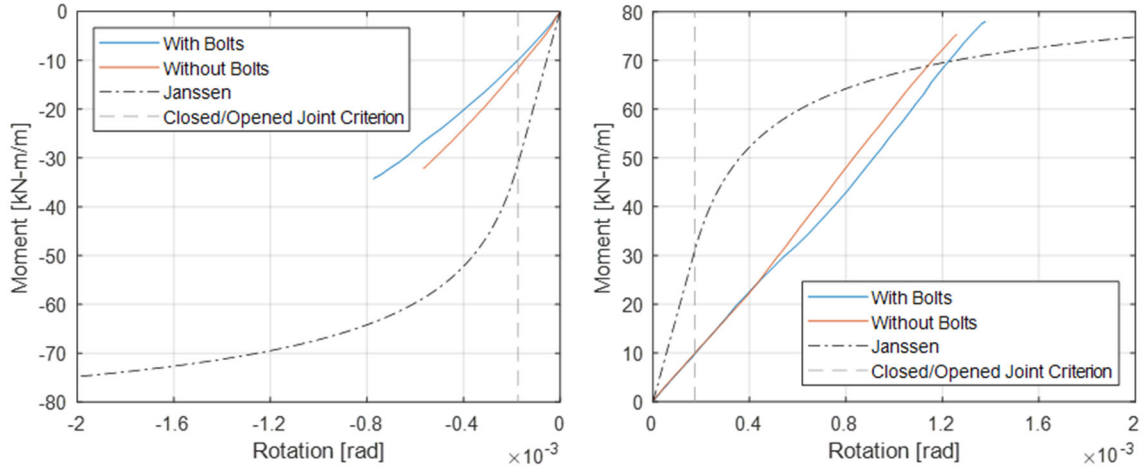

Figure 33: Negative and positive $M - \varphi$ curves for N = 674 kN/m axial force level

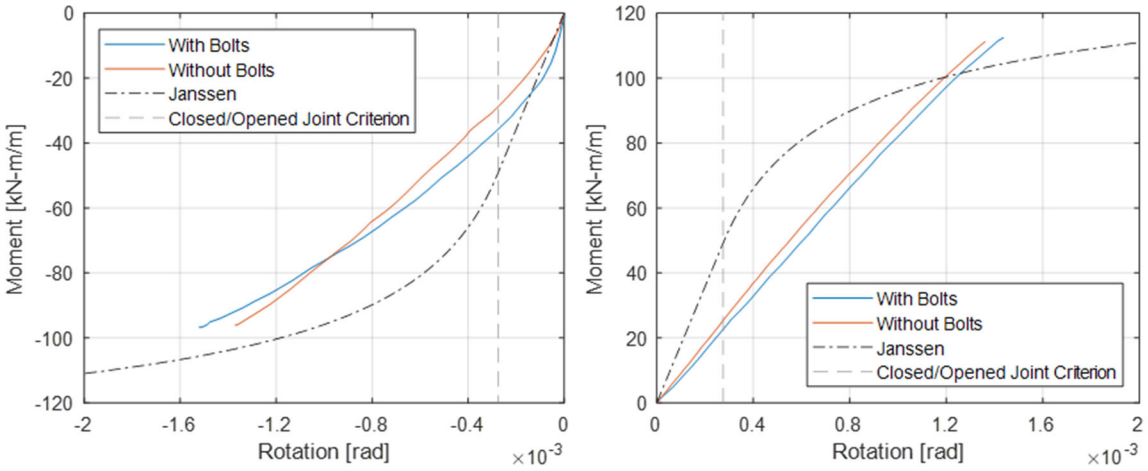

Figure 34: Negative and positive $M - \varphi$ curves at N = 1070 kN/m axial force level

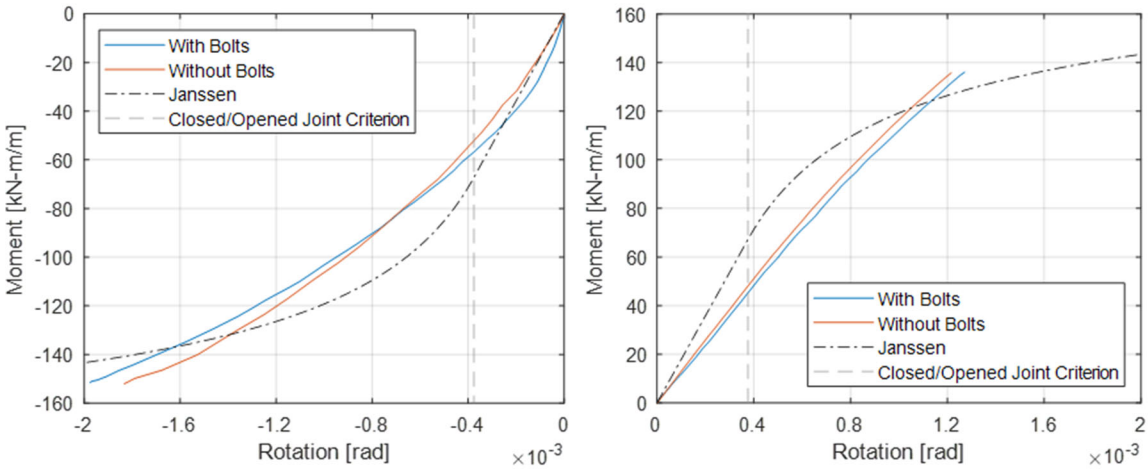

Figure 35: Negative and positive $M - \varphi$ curves at N = 1460 kN/m axial force level

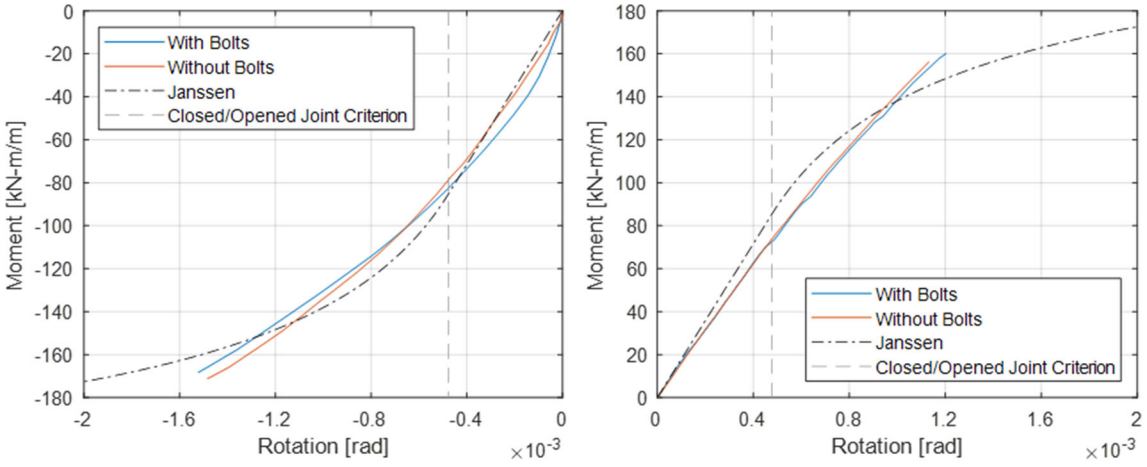

Figure 36: Negative and positive $M - \varphi$ curves at N = 1850 kN/m axial force level

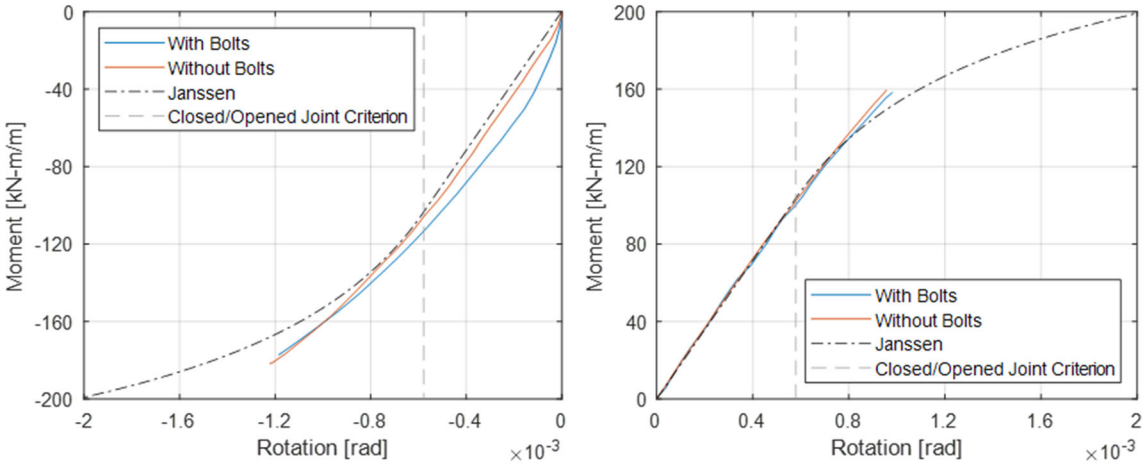

Figure 37: Negative and positive $M - \varphi$ curves at N = 2250 kN/m axial force level

Figure 38 and Figure 39 summarize the tangent rotational stiffness versus rotation based on the $M - \varphi$ results from Figure 33 to Figure 37. The positive $M - \varphi$ exhibits mild nonlinear behavior (mostly linear) while the negative $M - \varphi$ response exhibits a nonlinear, i.e., decreasing rotational stiffness with increasing rotation at early rotations less than the expected opening values. Slight as the variation exists, the radial joint generally exhibits similar rotational stiffness during $+M$ and $-M$ loading. The noted exception is at very low loads where rotational stiffness is greater during $-M$ loading than during similar magnitudes of $+M$ loading. Rotational stiffness increases considerably with increasing N during both $+M$ and $-M$ loading. This is evident both during full joint contact (closed joint) and partial contact (opened joint). The Janssen model predicts significantly different $M - \varphi$ response, especially at low axial load levels, including constant initial linear rotational stiffness before joint opening, and sudden decrease of rotational stiffness due to joint opening. Although the decrease of rotational stiffness is observed from experimental results, it is not as significant as Janssen's model where a clear twist can be seen. When at higher axial load levels, e.g. $N \geq 1850$ kN/m, Janssen's model gives reasonable prediction compared with the observed $M - \varphi$ response. Janssen's model does not predict the N-influenced initial joint rotational stiffness as what observed in the experimental results.

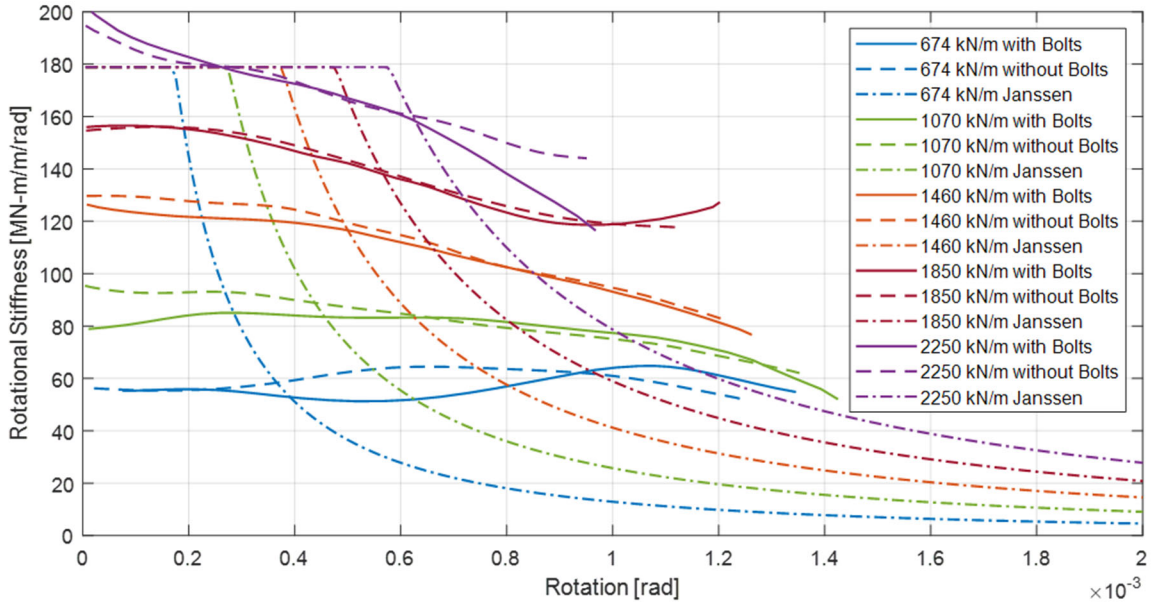

Figure 38: Positive rotational stiffness response of elastic testing

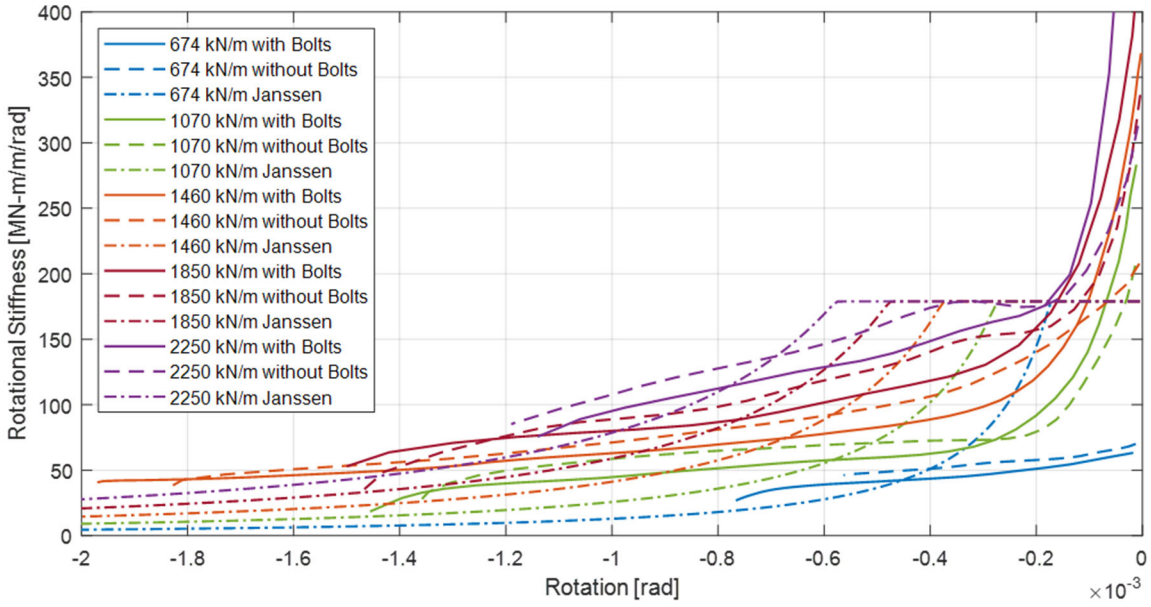

Figure 39: Negative rotational stiffness response of elastic testing

The assemblies with and without bolts generally exhibit similar $M - \varphi$ behavior. The use of bolts should conceptually increase the rotational stiffness since the bolt provides a spring resistance at an eccentricity from the compression face. The initial elastic rotational stiffness during loading of negative bending is greater with bolts, in all cases except for the low 674 kN/m axial load case. During loading for positive bending, however, the use of bolts results in a lower rotational stiffness. This is an unexpected result but can be contributed to the imperfect joint contact due to the nature of concrete. From mechanical perspective, this difference in rotational stiffness could also be associated with the location of the radial bolts relative to the compression zone in each bending direction. For example, since the bolts are located above the centroid of the contact surface, a

larger moment arm in the negative bending direction is presented than in the positive bending direction. This difference in moment arm may impact how they influence the rotation stiffness.

The secant rotational stiffness for each experimental case is determined. To be consistent the Janssen model, the rotational stiffness is determined at the expected joint opening rotation for each axial load level, as presented in Figure 33 to Figure 37. The rotation levels at which the stiffness values are determined are summarized in Table 9.

Table 9: Secant joint rotational stiffness

Axial load level (kN/m)	Expected Joint Rotation at Opening ($\times 10^{-3}$ rad)	Measured joint secant rotational stiffness [MN-m/m/rad]			
		$-M$ with bolts	$-M$ without bolts	$+M$ with bolts	$+M$ without bolts
674	0.174	57.1	66.8	56.3	57.4
1070	0.275	130	105	82.1	92.2
1460	0.376	151	139	120	128
1850	0.477	173	165	152	155
2250	0.587	196	183	173	176

The secant rotational stiffness for each axial load level is determined with and without bolts in both negative and positive bending and is plotted in Figure 40. The Janssen rotational stiffness of the joint at opening is independent of axial load and for the geometry and measured constitutive properties is estimated to be 179 MN-m/m/rad, per Equation 6. In comparison, the elastic stiffness of the SFRC segment is estimated to be 539 MN-m/m/rad, per Equation 8. As illustrated, the measured stiffness increases with axial load level. This behavior is not captured in the Janssen model. The stiffness values are also presented as relative to the Janssen model by plotting the ratio of measured joint rotational secant stiffness compared to theoretical solutions of joint stiffness and segment stiffness in Figure 41. Once the joint is open Janssen's model indicates that the rotational stiffness increases with higher axial force level, as expressed in Equation 7. At the highest axial load level, the secant joint rotational stiffness observed in large diameter testing was found to be greater than that predicted by the Janssen model.

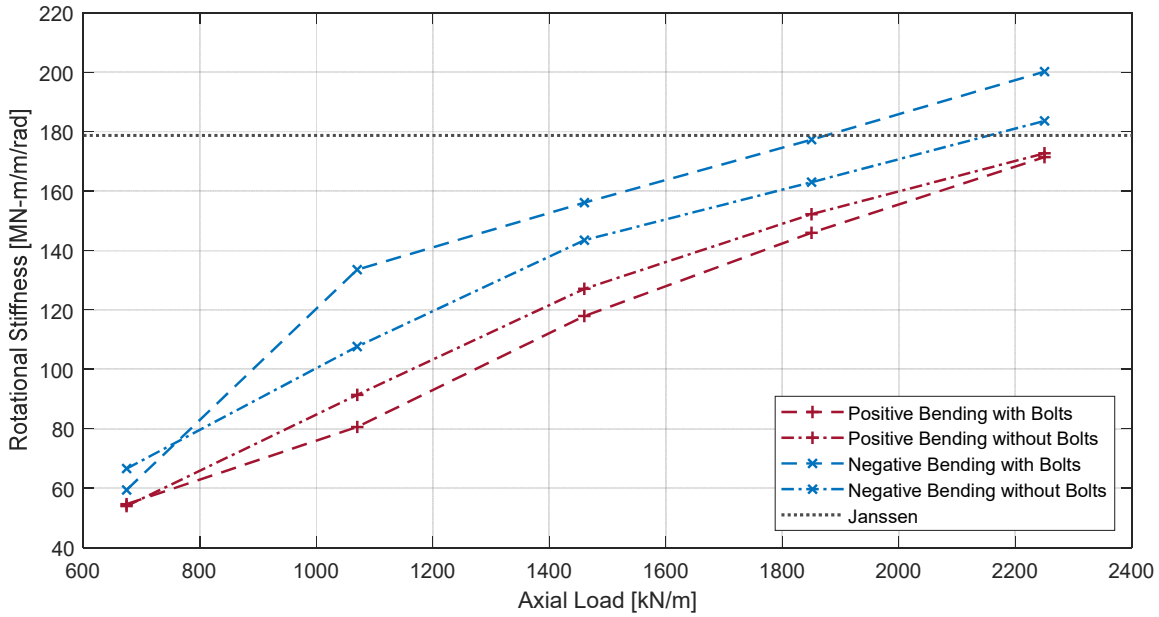

Figure 40: Secant Rotational stiffness at expected opening rotation under various axial load levels

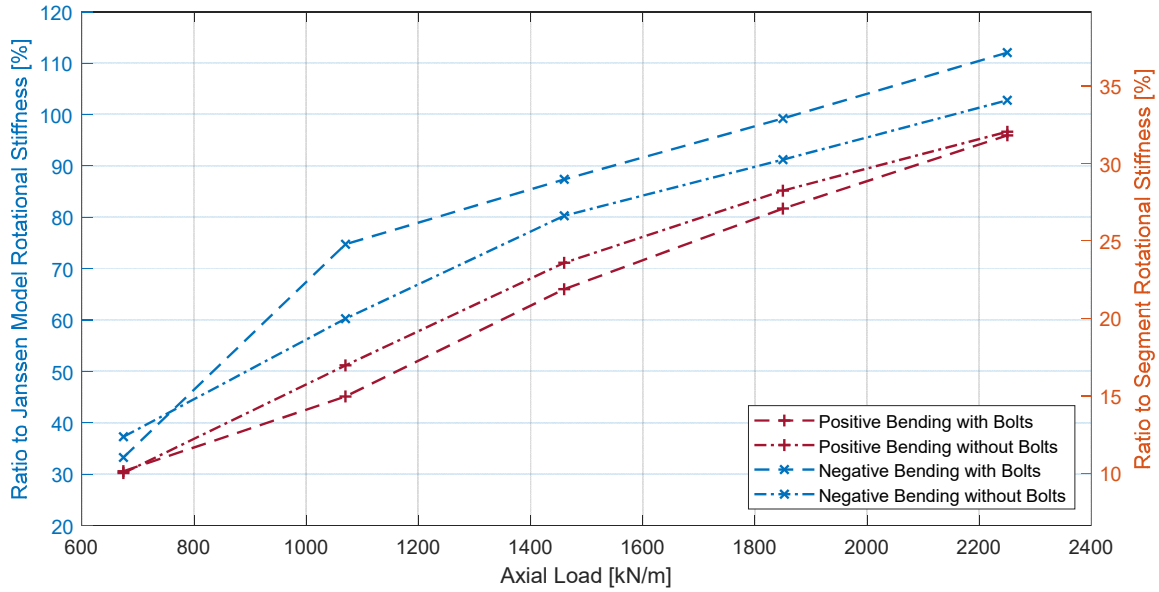

Figure 41: Ratio to the rotational stiffness of Janssen model and SFRC segment

3.5.2. Nonlinear-Inelastic Moment-Rotation Assessment

The positive $M - \varphi$ behavior at three axial force levels is plotted in Figure 42. These tests were conducted to large joint rotation significantly greater than the assumed rotation at joint opening. Note that the same assembly with bolts under an axial load of 674 kN/m was tested after examination of joint rotational behavior with bolts under 1460 kN/m axial load, for the initial rotational stiffness was not compromised compared to the experimental results of initial joint rotational stiffness from Chapter 3.5.1. At 1460 kN/m axial load level, the effects of bolting at

large rotation were also examined. The tangent rotational stiffness was computed through the rotation history and compared with Janssen's model. As shown in Figure 43, the initial measured stiffness is lower than Janssen but becomes greater than the model at rotations greater than approximately 0.001 rad. The theoretical solutions based on Janssen's model are also plotted. The experimental results reveal considerably greater eventual joint flexural capacity than is estimated by Janssen's model. The tests were stopped when the response exhibited low rotational stiffness due to stability concerns in the laboratory.

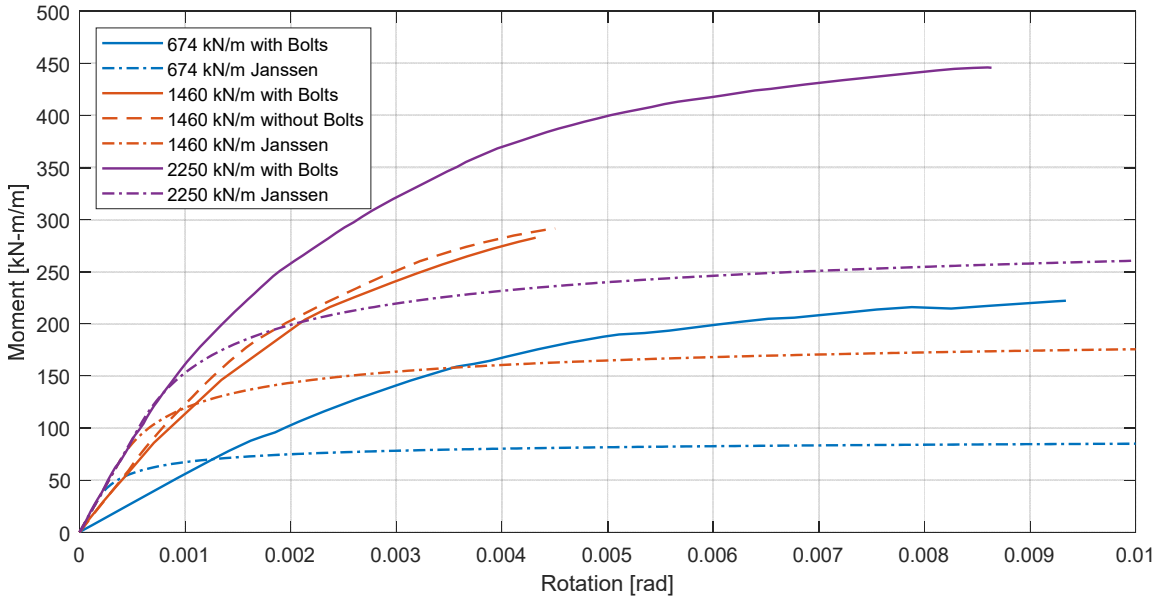

Figure 42: Moment-rotation response to large rotation levels

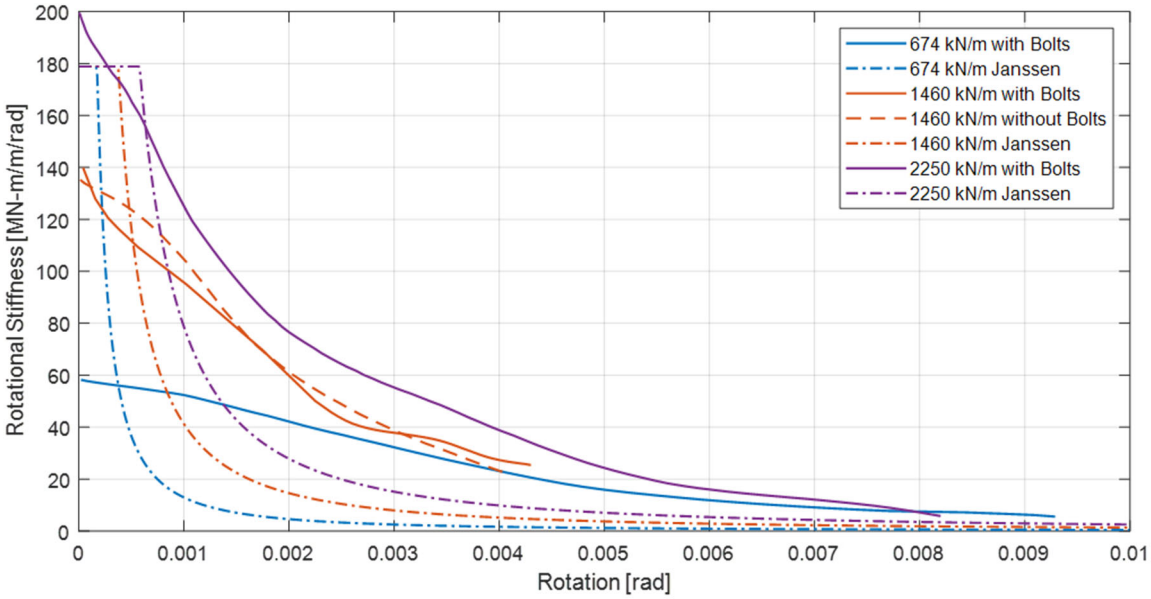

Figure 43: Rotational stiffness response to large rotation levels

From the Janssen model, during nonlinear-inelastic response, the joint rotational behavior is controlled by the axial force at the joint, and the rotational stiffness generally increases with the

axial force. The phenomenon of axial load controlled joint rotational behavior is evidently observed in experimental results. The difference between experimental results and Janssen's theoretical solutions becomes less significant when the axial load is higher. As shown in Figure 42, the moment asymptotes of experimental results are significantly higher than the moment asymptotes of Janssen's theoretical solutions, indicating the joint has higher flexural capacity at large rotation than predicted values. This could be associated with that 1) the rotational behavior of skewed joints involved with both segments and radial joint along circumferential direction; 2) the joint contact depth, X_u, is larger than predicted using Janssen's solution due to concrete plasticity and effects of confined concrete (*57*).

As shown in Figure 43, the rotational stiffness from experimental results start to be higher than Janssen's theoretical solution when $\varphi > 0.0005$ rad, and the difference becomes more significant at large rotation, until $\varphi = 0.004$. This phenomenon can be contributed to that the skewed joint restrain the joint opening, as the joint is only aligned with the radius direction at $^{b}/_{2}$ and the entire skewed joint is parallel to the radius direction at $^{b}/_{2}$, causing skewness along radial (i.e. thickness) direction as well, other than the 8° skewness in tunnel longitudinal direction. As presented in previous section, bolts lead to slightly lower rotational stiffness, which can be recognize at large rotation level as shown in Figure 43. However, at large rotation level of 0.003 rad, the rotational stiffness of the assembly with bolts start to become higher than the assembly without bolts. It is concluded that bolts can benefit rotational behavior only at large rotation level.

3.5.3. Joint Damage Assessment

The behavior of damaged joints under the negative bending moment was examined at axial force levels of 1460 and 2250 kN/m following the previous nonlinear-inelastic testing. The moment-rotation responses of joints after potential damage from previous inelastic testing are summarized in Figure 44 with the results from Chapter 3.5.1. The rotational stiffness versus rotation was computed and plotted in Figure 45. At maximum allowable rotation for single joint, 0.00684 rad, the $M - \varphi$ response and rotational stiffness are similar for both the cases. The damage from previous only likely to affect the initial rotational stiffness. The rotational assessment on damaged joints shows that the local damage caused by positive bending moment can affect the initial rotational behavior when subjected to negative bending moment. The effect of potential damage is less significant when the reaction force, R (Figure 22), moves towards the undamaged area.

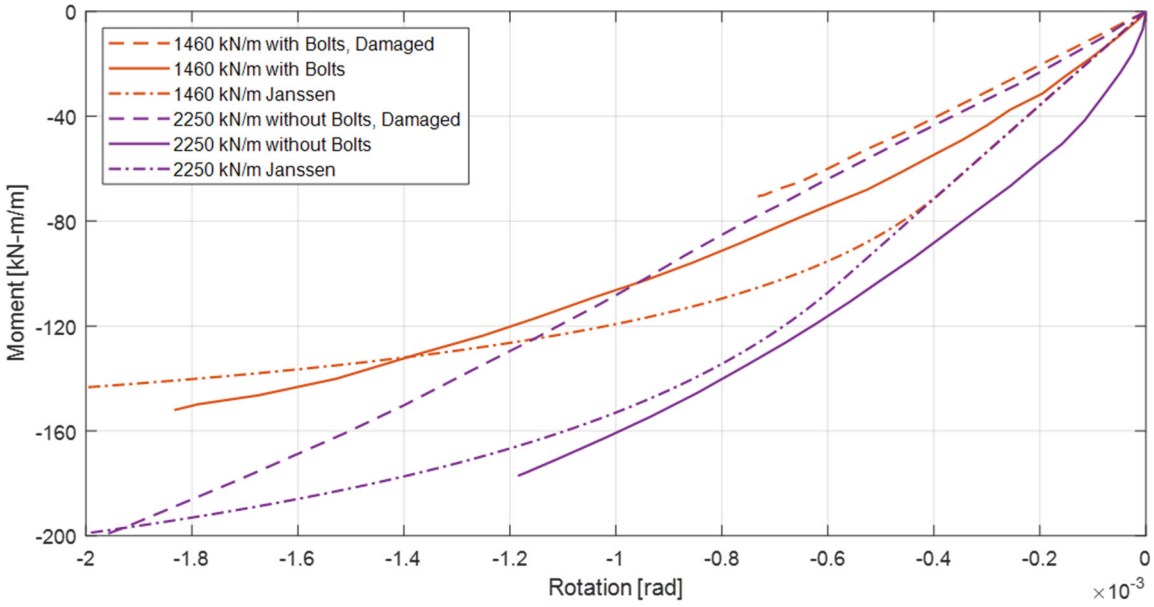

Figure 44: Moment-rotation response after damaged by previous inelastic testing

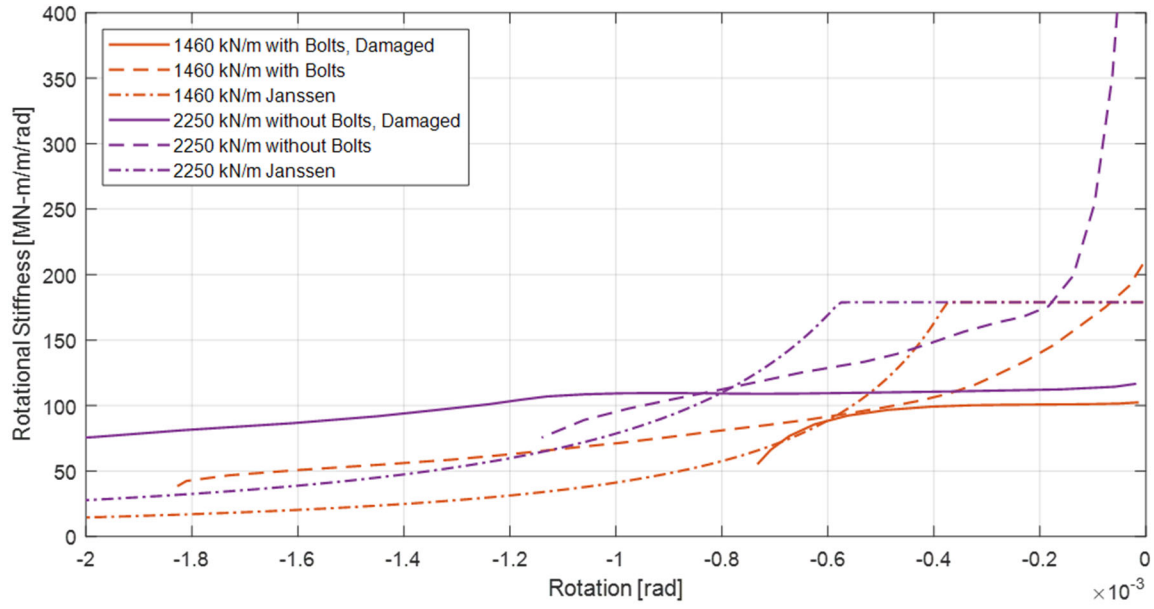

Figure 45: Rotational stiffness response after damaged by previous inelastic testing

Following the test, the assembly was taken apart and photos of the radial joint contact surfaces were taken and compared with the photos taken before testing. The post-test visible damage to the joint for each case was minimal, and no post-test damage was found on other surfaces, e.g. circumferential joints, cut faces, intrados and extrados surfaces. Radial joint damage consisted of hairline cracking (less than 0.1 mm) at the compression face of the contact area. Localized cracks greater than 0.1 mm were observed around the radial bolts as illustrated in Figure 46. Damage only occurred within the joint face, thus observations of when they occurred were not available.

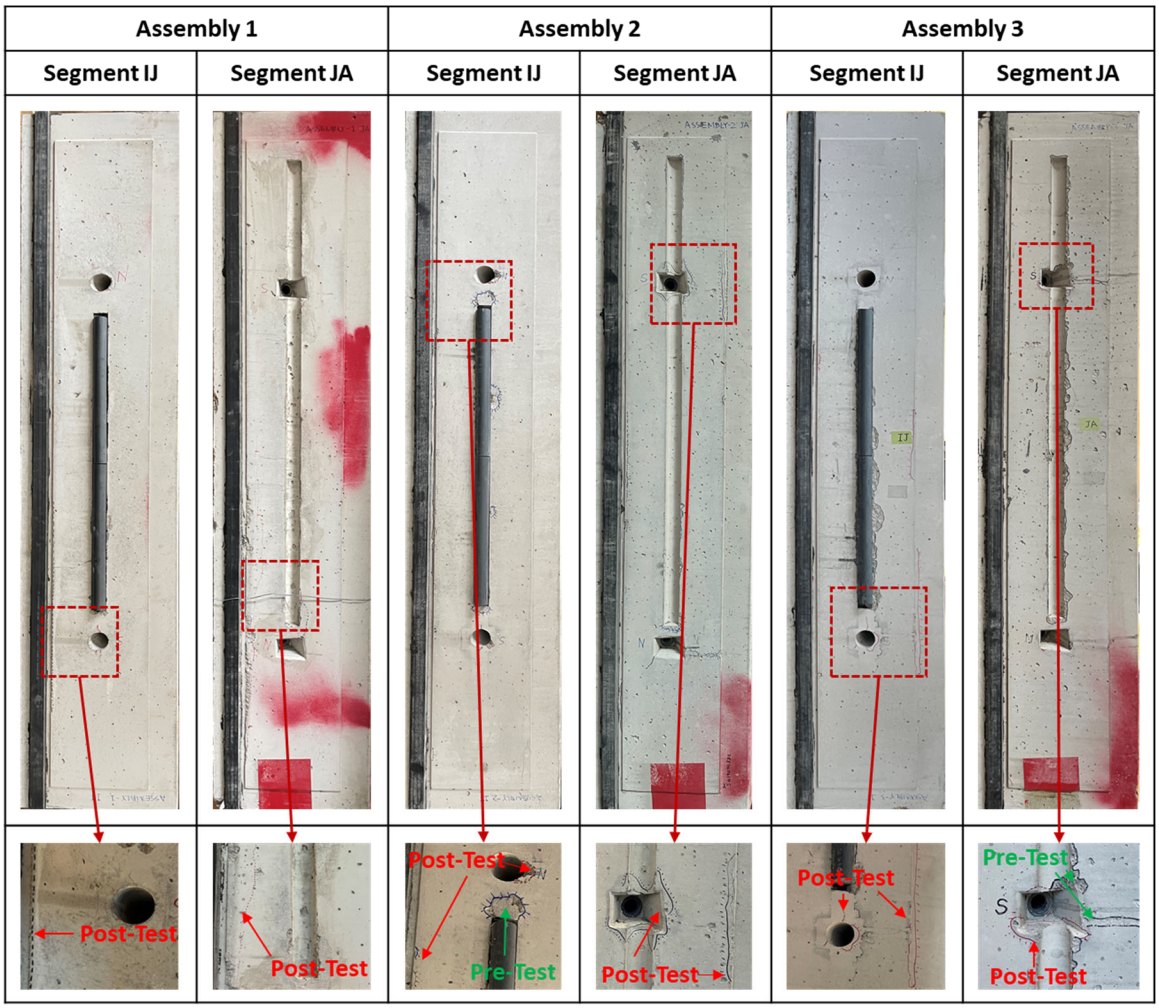

Figure 46: Post-test damage observations on joint

3.6. Conclusions

A series of tests were performed on skewed radial joint assemblies. The rotational behaviors under various axial load levels and the effects of bolting were explored experimentally. Potential joint damage due to excessive rotation was also assessed. Based on the results of the experimental program and the comparison to the Janssen's theoretical solutions, the following conclusions can be made:

- The Janssen model idealizes the joint contact, thus overestimates the rotational stiffness of closed joints when subjected to low axial load. At relatively large rotation level, Janssen's theoretical solutions provide overly conservative estimation of rotational stiffness and ultimate flexural capacity. It is important to note that the joint used in this study represents a typical perpendicular tunnel joint connection and includes both radial bolts and a gasket

that are required for construction of tunnels but not directly considered in the Janssen model. For better approximation through computational joint model, the aforementioned factors, e.g. skewness, bolts, gasket, effects of confined concrete, and the relationship between joint contact and axial force levels, should be considered.

- The measured elastic positive and negative moment–rotation responses and rotational stiffness of the radial joint observed was similar at rotations close to the joint opening, with or without bolting. The use of bolts alters the rotational stiffness of the joint slightly; however, the change in behavior due to bolting is minimal at small rotation. From experimental results, bolting can provide significant rotational stiffness at large joint rotation level. The bolts can be removed when the tunnel construction is complete; however, it is suggested to reserve the bolts at the joint locations where might experience large rotation due to earth pressure and other types of loading.
- Compared to the experimental results from available study with similar but perpendicular radial joints (*49*) and Janssen's model, the flexural capacity of perpendicular joint is approximately 10% higher than predicted in Janssen's model when subjected to an axial load of 1890 kN/m. Nevertheless, the flexural capacities of skewed radial joints are also approximately 80% higher than predicted in Janssen's model when subjected to the axial loads of 1460 and 2250 kN/m. The experimental results are significantly higher than perpendicular radial joints as well as Janssen's model.
- The damage to the joint at large rotations (0.004 to 0.010 rad) is limited to hairline cracking of the contact surface. No damage would be visible on the intrados under these elevated demands thus limiting the potential for in-situ inspection.

- It is worth to point out that the stiffness can be affected by the adjacent rings due to relatively high compressive force on circumferential joints. The stiffness can also be affected by the layout of adjacent segments from the adjacent rings, e.g. staggered/non-staggered joints (*43*) (*52*).

4. Fire Induced Spall of Full-Scale Liners

4.1. Introduction and Background

The fire resistance of as-built tunnel segments were examined through experimental testing. Segments from the same tunnel examined in earlier sections of this report were procured and setup for fire evaluation.

4.2. Test Setup

The tests were conducted using a gas fired radiant heat panel which was ignited and moved to the correct standoff distance within a 5 second period. The setup is shown Figure 47 with the full-scale panel.

Figure 47: Large panel fire test

Temperature measurements were taken using post-installed thermocouples mounted from the intrados face as shown in Figure 48 Figure 49. Data was recorded through spalling.

Figure 48: Thermocouple installation

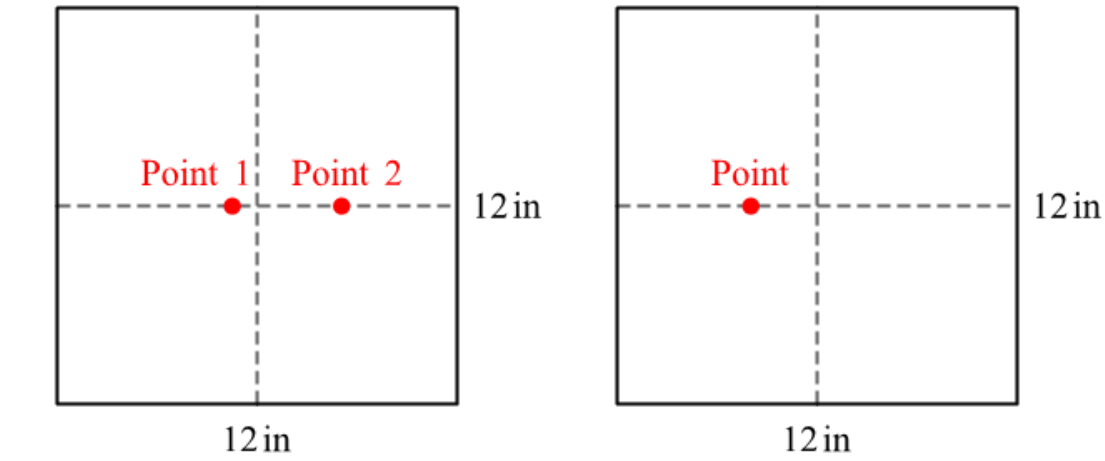

Figure 49: Thermocouple placement relative to radiant panel center, (a) Panel 1 Point 1 Point 1: 0.25in to the center, hole depth 4mm, Point 2: 2.75in to the center, hole depth 4mm, (b) Panel 2 Point: 1.5in to the center, hole depth 4.5mm

4.3. Spall results

The moisture content and lab temperature was measured prior to testing. Panel 1 had a measured moisture content of 3.6% and 17.3C air temperature, Panel 2 had a moisture content of 3.8% and an air temperature of 16.5C. Both panels spalled within 2 minutes of thermal exposure. The spall initiation can be seen from the jump in the measured temperatures on the embedded thermocouples. Panel 1 exhibits a jump at 1.8 minutes and panel 2 starts just prior to 2 minutes. The tests were characterized by a continuous loss of concrete. Panel test 1 was stopped at 5 minutes and panel test 2 was stopped after 2.6 minutes. The tests were stopped after these short durations to prevent damage to the radiant panel. The measured temperatures at the thermocouples are presented in Figure 50. The post fire damage is shown in Figure 51 and Figure 52.

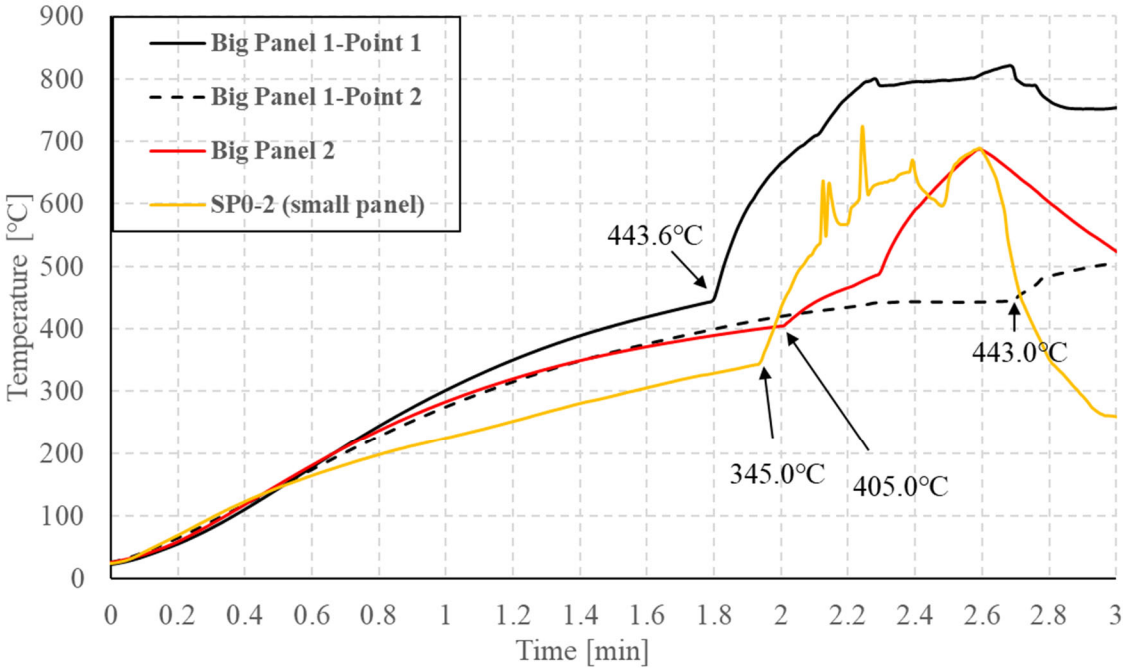

Figure 50: Thermocouple measurements

Figure 51: Panel 1 post test

Figure 52: Panel 2 post test

4.4. Conclusions

The fire exposure of the intrados surface of the SFRC tunnel liner segments resulted in temperature induced spall. The spall depth increased with continued thermal demand and can lead to significant damage under a fire event. The steel fibers did not prevent spall and while one end of the fiber typically remained embedded in the concrete, the other end on the spalled section did not prevent the concrete from separating from the liner.

References

1. Janssen, P. *Tragverhalten von Tunnelausbauten mit Gelenktübbings*. Ph.D. Thesis. Technische Universität Braunschweig, Braunschweig, Germany, 1983.
2. ACI Committee 544. *ACI 544.7R-16 Report on Design and Construction of Fiber-Reinforced Precast Concrete Tunnel Segments*. American Concrete Institute, Farmington Hills, MI, 2016.
3. Bakhshi, M., and V. Nasri. Design Considerations for Precast Tunnel Segments According to International Recommendations, Guidelines and Standards. Presented at the Vancouver TAC 2014: Tunnelling in a Resource Driven World, Vancouver Canada, 2014.
4. Breen, J. E., O. Burdet, C. Roberts, D. Sanders, and G. Wollmann, Eds. *Anchorage Zone Reinforcement for Post-Tensioned Concrete Girders*. Transportation Research Board, National Research Council : National Academy Press, Washington, D.C, 1994.
5. Iyengar, K. T. S. R. Two-Dimensional Theories of Anchorage Zone Stresses in Post-Tensioned Prestressed Beams. *Journal Proceedings*, Vol. 59, No. 10, 1962, pp. 1443–1466. https://doi.org/10.14359/7961.
6. Conforti, A., G. Tiberti, and G. A. Plizzari. Combined Effect of High Concentrated Loads Exerted by TBM Hydraulic Jacks. *Magazine of Concrete Research*, Vol. 68, No. 21, 2016, pp. 1122–1132. https://doi.org/10.1680/jmacr.15.00430.
7. Groeneweg, T. *Shield Driven Tunnels in Ultra High Strength Concrete - Reduction of the Tunnel Lining Thickness*. PhD Thesis. Delft University of Technology, 2007.
8. ACI Committee 544. *ACI 544.8R-16 Report on Indirect Method to Obtain Stress-Strain Response of Fiber-Reinforced Concrete (FRC)*. American Concrete Institute, Farmington Hills, Mich., 2016.
9. ITA Working Group 2. *Guidelines for the Design of Segmental Tunnel Linings*. Publication 978-2-9701242-1–4. International Tunnelling Association, Longrine, France, 2019, p. 59.
10. AASHTO. *LRFD Road Tunnel Design and Construction Guide Specifications*. American Association of State Highway and Transportation Officials, Washington, DC., 2017.
11. Winterberg, R., and T. Clarke. Performance of Tunnel Segments Reinforced with Synthetic Macro Fibers. Presented at the Proceedings of the World Tunnel Congress, 2021.
12. Liao, L., A. de la Fuente, S. Cavalaro, and A. Aguado. Design of FRC Tunnel Segments Considering the Ductility Requirements of the Model Code 2010. *Tunnelling and Underground Space Technology*, Vol. 47, 2015, pp. 200–210. https://doi.org/10.1016/j.tust.2015.01.006.
13. Caratelli, A., A. Meda, Z. Rinaldi, and P. Romualdi. Structural Behaviour of Precast Tunnel Segments in Fiber Reinforced Concrete. *Tunnelling and Underground Space Technology*, Vol. 26, No. 2, 2011, pp. 284–291. https://doi.org/10.1016/j.tust.2010.10.003.
14. International Federation for Structural Concrete. *Fib Model Code for Concrete Structures 2010*. International Federation for Structural Concrete (fib), Lausanne, Switzerland, 2013.
15. Abbas, S. *Structural and Durability Performance of Precast Segmental Tunnel Linings*. Ph.D. Thesis. The University of Western Ontario, Canada, 2014.
16. Hilar, M., J. L. Vitek, and R. Pukl. Laboratory Testing and Numerical Modelling of Sfrc Tunnel Segments. Presented at the Eastern European Tunnelling Congress, Budapest, Hungary, 2012.
17. Beňo, J., and M. Hilar. Steel Fibre Reinforced Concrete for Tunnel Lining – Verification by Extensive Laboratory Testing and Numerical Modelling. *Acta Polytechnica*, Vol. 53, No. 4, 2013. https://doi.org/10.14311/1823.

18. Conforti, A., G. Tiberti, G. A. Plizzari, A. Caratelli, and A. Meda. Precast Tunnel Segments Reinforced by Macro-Synthetic Fibers. *Tunnelling and Underground Space Technology*, Vol. 63, 2017, pp. 1–11. https://doi.org/10.1016/j.tust.2016.12.005.
19. Conforti, A., I. Trabucchi, G. Tiberti, G. A. Plizzari, A. Caratelli, and A. Meda. Precast Tunnel Segments for Metro Tunnel Lining: A Hybrid Reinforcement Solution Using Macro-Synthetic Fibers. *Engineering Structures*, Vol. 199, 2019, p. 109628. https://doi.org/10.1016/j.engstruct.2019.109628.
20. Burgers, R., J. Walraven, G. A. Plizzari, and G. Tiberti. Structural Behavior of SFRC Tunnel Segments during TBM Operations. 2007.
21. Krahl, P. A., I. I. Palomo, S. J. de C. Almeida, G. Henrique Siqueira, N. de O. Pinto Júnior, and L. C. M. Vieira Junior. Tolerances for TBM Thrust Load Based on Crack Opening Performance of Fiber-Reinforced Precast Tunnel Segments. *Tunnelling and Underground Space Technology*, Vol. 111, 2021, p. 103847. https://doi.org/10.1016/j.tust.2021.103847.
22. Nogales, A., and A. de la Fuente. Crack Width Design Approach for Fibre Reinforced Concrete Tunnel Segments for TBM Thrust Loads. *Tunnelling and Underground Space Technology*, Vol. 98, 2020, p. 103342. https://doi.org/10.1016/j.tust.2020.103342.
23. Trabucchi, I., G. Tiberti, and G. A. Plizzari. A Parametric Numerical Study on the Behavior of Large Precast Tunnel Segments during TBM Thrust Phase. *Engineering Structures*, Vol. 241, 2021, p. 112253. https://doi.org/10.1016/j.engstruct.2021.112253.
24. ASTM Standard A820-16. *Specification for Steel Fibers for Fiber-Reinforced Concrete*. ASTM International, West Conshohocken, PA, 2016.
25. CEN. *Fibres for Concrete - Part 1: Steel Fibres - Definitions, Specifications and Conformity*. Publication EN 14889-1:2006. European Committee for Standardization, Brussels, Belgium, 2006.
26. ISO. *ISO 13270:2013 Steel Fibres for Concrete — Definitions and Specifications*. Publication ISO 13270:2013. International Organization for Standardization, 2013.
27. ASTM Standard C39-20. *Test Method for Compressive Strength of Cylindrical Concrete Specimens*. ASTM International, West Conshohocken, PA, 2020.
28. ASTM Standard C469-14. *Standard Test Method for Static Modulus of Elasticity and Poisson's Ratio of Concrete in Compression*. ASTM International, West Conshohocken, PA, 2014.
29. Graybeal, B., and F. Baby. Development of Direct Tension Test Method for Ultra-High-Performance Fiber-Reinforced Concrete. *ACI Materials Journal*, No. 110, 2013, pp. 177–186. https://doi.org/10.14359/51685532.
30. ASTM Standard C496-17. *Test Method for Splitting Tensile Strength of Cylindrical Concrete Specimens*. ASTM International, West Conshohocken, PA, 2017.
31. CEN. *Test Method for Metallic Fibered Concrete - Measuring the Flexural Tensile Strength*. Publication EN 14651-2005. European Committee for Standardization, Brussels, Belgium, 2005.
32. Abrishambaf, A., J. A. O. Barros, and V. M. C. F. Cunha. Tensile Stress–Crack Width Law for Steel Fibre Reinforced Self-Compacting Concrete Obtained from Indirect (Splitting) Tensile Tests. *Cement and Concrete Composites*, Vol. 57, 2015, pp. 153–165. https://doi.org/10.1016/j.cemconcomp.2014.12.010.
33. Shen, Q., W. Chen, C. Liu, W. Zou, and L. Pan. The Tensile Strength and Damage Characteristic of Two Types of Concrete and Their Interface. *Materials*, Vol. 13, No. 1, 2020, p. 16. https://doi.org/10.3390/ma13010016.

34. Stephen, S. J., B. Raphael, R. Gettu, and S. Jose. Determination of the Tensile Constitutive Relations of Fiber Reinforced Concrete Using Inverse Analysis. *Construction and Building Materials*, Vol. 195, 2019, pp. 405–414. https://doi.org/10.1016/j.conbuildmat.2018.11.014.
35. RILEM TC 162-TDF. Final Recommendation of RILEM TC 162-TDF: Test and Design Methods for Steel Fibre Reinforced Concrete: σ-ε Design Method. *Materials and Structures*, Vol. 36, 2003.
36. Olesen, J. F. Fictitious Crack Propagation in Fiber-Reinforced Concrete Beams. *Journal of Engineering Mechanics*, Vol. 127, No. 3, 2001, pp. 272–280. https://doi.org/10.1061/(ASCE)0733-9399(2001)127:3(272).
37. Barros, J. A. O., V. M. C. F. Cunha, A. F. Riberiro, and Antunes. Post-Cracking Behaviour of Steel Fibre Reinforced Concrete. *Materials and Structures*, Vol. 38, No. 275, 2004, pp. 47–56. https://doi.org/10.1617/14058.
38. ASTM Standard A615-18. *Specification for Deformed and Plain Carbon-Steel Bars for Concrete Reinforcement*. ASTM International, West Conshohocken, PA, 2018.
39. ACI Committee 318. *ACI 318-19: Building Code Requirements for Structural Concrete and Commentary*. American Concrete Institute, Farmington Hills, MI, 2019.
40. Dassault Systèmes. Abaqus/CAE 2020. Dassault Systemes Simulia Corp., Johnston, RI, USA, Sep 13, 2019.
41. Iyengar, K. T. S. R. *Der Spannungszustand in Einem Elastischen Halbstreifen Und Seine Technischen Anwendungen*. Dissertation. Technische Hochschule, Hannover, 1960.
42. Liu, X., Y. Zhang, Y. Bao, and W. Song. Investigation of the Structural Effect Induced by Stagger Joints in Segmental Tunnel Linings: Numerical Explanation via Macro-Level Structural Modeling. *Tunnelling and Underground Space Technology*, Vol. 120, 2022, p. 104284. https://doi.org/10.1016/j.tust.2021.104284.
43. Mooney, M., T. Epel, A. Wilson, H. Zheng, and A. G. Nitschke. Experimental Behavior of Large Diameter Segmental Lining Systems: A Review. 2020.
44. Liu, X., Y. Bai, Y. Yuan, and H. A. Mang. Experimental Investigation of the Ultimate Bearing Capacity of Continuously Jointed Segmental Tunnel Linings. *Structure and Infrastructure Engineering*, Vol. 12, No. 10, 2016, pp. 1364–1379. https://doi.org/10.1080/15732479.2015.1117115.
45. Nakamura, H., T. Kubota, M. Furukawa, and T. Nakao. Unified Construction of Running Track Tunnel and Crossover Tunnel for Subway by Rectangular Shape Double Track Cross-Section Shield Machine. *Tunnelling and Underground Space Technology*, Vol. 18, No. 2–3, 2003, pp. 253–262. https://doi.org/10.1016/S0886-7798(03)00034-8.
46. Blom, C. B. M., E. J. van der Horst, and P. S. Jovanovic. Three-Dimensional Structural Analyses of the Shield-Driven "Green Heart" Tunnel of the High-Speed Line South. *Tunnelling and Underground Space Technology*, Vol. 14, No. 2, 1999, pp. 217–224. https://doi.org/10.1016/S0886-7798(99)00035-8.
47. Liang Lu, Xilin Lu, and Peifang Fan. Full-Ring Experimental Study of the Lining Structure of Shanghai Changjiang Tunnel. *Journal of Civil Engineering and Architecture*, Vol. 5, No. 8, 2011. https://doi.org/10.17265/1934-7359/2011.08.007.
48. Zuo, L., G. Li, K. Feng, X. Ma, L. Zhang, Y. Qiu, S. Cao, and L. Feng. Experimental Analysis of Mechanical Behavior of Segmental Joint for Gas Pipeline Shield Tunnel under Unfavorable Compression-Bending Loads. *Tunnelling and Underground Space Technology*, Vol. 77, 2018, pp. 227–236. https://doi.org/10.1016/j.tust.2018.03.005.

49. Chen, Z., Z. Yang, and D. Li. Experimental Study on Mechanical Properties of Longitudinal Seam of Shanghai Changjiang Shield Tunnel. *Underground Engineering and Tunnels*, Vol. 4, 2010, pp. 17–19.
50. Jin, Y., W. Ding, Z. Yan, K. Soga, and Z. Li. Experimental Investigation of the Nonlinear Behavior of Segmental Joints in a Water-Conveyance Tunnel. *Tunnelling and Underground Space Technology*, Vol. 68, 2017, pp. 153–166. https://doi.org/10.1016/j.tust.2017.05.018.
51. Li, X., Z. Yan, Z. Wang, and H. Zhu. Experimental and Analytical Study on Longitudinal Joint Opening of Concrete Segmental Lining. *Tunnelling and Underground Space Technology*, Vol. 46, 2015, pp. 52–63. https://doi.org/10.1016/j.tust.2014.11.002.
52. Liu, X., Z. Dong, W. Song, and Y. Bai. Investigation of the Structural Effect Induced by Stagger Joints in Segmental Tunnel Linings: Direct Insight from Mechanical Behaviors of Longitudinal and Circumferential Joints. *Tunnelling and Underground Space Technology*, Vol. 71, 2018, pp. 271–291. https://doi.org/10.1016/j.tust.2017.08.030.
53. Liu, X., C. Zhang, C. Zhang, and Y. Yuan. Ultimate Load-Carrying Capacity of the Longitudinal Joints in Segmental Tunnel Linings. *Structural Concrete*, Vol. 18, No. 5, 2017, pp. 693–709. https://doi.org/10.1002/suco.201600070.
54. Zhang, J., and M. Zhao. Experimental Study on Mechanical Behavior of the Skew Joints of Shield Tunnels under Large Eccentric Compressive Loading. *Tunnelling and Underground Space Technology*, Vol. 111, 2021, p. 103876. https://doi.org/10.1016/j.tust.2021.103876.
55. Vardakos, S., A. Nitschke, and M. Mooney. *Precast Concrete Segmental Liners for Large Diameter Highway Tunnels - Workshop Report*. Publication FHWA-HIF-20-036. Federal Highway Administration, WSP USA, Inc. One Penn Plaza 250 West 34th Street New York, NY, 10119, 2020, p. 46.
56. Blom, C. B. M. *Lining Behaviour-Analytical Solutions of Coupled Segmented Rings in Soil*. Delft University of Technology, 2002.
57. Tvede-Jensen, B., M. Faurschou, and T. Kasper. A Modelling Approach for Joint Rotations of Segmental Concrete Tunnel Linings. *Tunnelling and Underground Space Technology*, Vol. 67, 2017, pp. 61–67. https://doi.org/10.1016/j.tust.2017.04.019.

Appendix A: Technology Transfer Activities

1 Accomplishments

Design approaches for thrust and joint flexure of tunnel liners developed. Spall sensitivity of liners subject to fire demonstrated.

1.1 What was done? What was learned?

(1) The design approach for thrust application on precast tunnel liner segments were examined and new recommendations were developed.

(2) The design approach for flexural joint rotation of precast tunnel liner radial joints were examined and new recommendations were developed.

(3) The fire resistance of tunnel segments were demonstrated.

1.2 How have the results been disseminated?

- Publications have been written and are under review.

2 Participants and Collaborating Organizations

Name: Lehigh University

Location: Bethlehem, PA

Contribution: Colorado School of Mines

3 Outputs

Journal publications

- Ouyang, Z., Naito, C., Quiel, S., Mooney, M., "Strain-Based Design Approach for Precast Fiber Reinforced Concrete Tunnel Lining Segments Under Thrust Jack Loading," Submitted to Journal of Tunnelling and Underground Space Technology incorporating Trenchless Technology Research, Manuscript Number TUST-D-23-01231, July 2023.

- Ouyang, Z., Haotian, Z., Naito, C., Quiel, S., Mooney, M., "Testing of Axial-Moment-Rotation Response for Skewed Flat Radial Joints in Precast Concrete Segmental Tunnel Linings," Submitted to Journal of Tunnelling and Underground Space Technology incorporating Trenchless Technology Research, Manuscript Number TUST-S-23-03121, December 2023.

Workshops

- None

4 Outcomes

- New design methods for tunnel liners

5 Impacts

- Design approach to be discussed at ACI meetings for possible inclusion in upcoming design codes.

Appendix B: Data from the Project

All data available on request.